Report Title: **Hafnia-Based Nanostructured Thermal Barrier Coatings for Advanced Hydrogen Turbine Technology**

Principal Investigator: **Chintalapalle V. Ramana, Ph.D.**
Department of Mechanical Engineering
The University of Texas at El Paso
500 West University Ave.
El Paso, Texas 79968
Tel: 9157478690; Fax 9157475019
E-mail: rvchintalapalle@utep.edu

Co-Investigator: **Ahsan R. Choudhuri, Ph.D.**
Department of Mechanical Engineering
The University of Texas at El Paso
500 West University Ave.
El Paso, Texas 79968
Tel: 9157475450; Fax 9157475019
E-mail: ahasn@utep.edu

Report Type: Final Technical Report
Period: 10/01/2010 to 04/30/2013
Date of Report: June 1, 2013

Report submitted to: Department of Energy, National Energy Technology Laboratory

ABSTRACT

Thermal barrier coatings (TBCs) are critical technologies for future gas turbine engines of advanced coal based power generation systems. TBCs protect engine components and allow further increase in engine temperatures for higher efficiency. In this work, nanostructured HfO_2-based coatings, namely Y_2O_3-stabilized HfO_2 (YSH), Gd_2O_3-stabilized HfO_2 (GSH) and Y_2O_3-stabilized ZrO_2-HfO_2 (YSZH) were investigated for potential TBC applications in hydrogen turbines. Experimental efforts are aimed at creating a fundamental understanding of these TBC materials. Nanostructured ceramic coatings of YSH, GSH and YSZH were grown by physical vapor deposition methods. The effects of processing parameters and ceramic composition on the microstructural evolution of YSH, GSH and YSZH nanostructured coatings was studied using combined X-ray diffraction (XRD) and Electron microscopy analyses. Efforts were directed to derive a detailed understanding of crystal-structure, morphology, and stability of the coatings. In addition, thermal conductivity as a function of composition in YSH, YSZH and GSH coatings was determined. Laboratory experiments using accelerated test environments were used to investigate the relative importance of various thermo-mechanical and thermo-chemical failure modes of TBCs. Effects of thermal cycling, oxidation and their complex interactions were evaluated using a syngas combustor rig.

EXECUTIVE SUMMARY

Thermal barrier coatings (TBCs) are critical for future gas turbines of advanced coal based power generation systems. Future generation gas turbine engines should tolerate fuel compositions ranging from natural gas to a broad range of syngas with high hydrogen contents which require TBCs with a surface temperature tolerance much higher than the current standard materials. A place to look for alternative, next-generation thermal barrier coating (TBC) materials with superior properties is among fluorite structure oxides, where HfO_2 and ZrO_2 are the most suitable candidates. The melting point of HfO_2 is higher than ZrO_2 and yttria stabilized hafnia (YSH) has a durability to a temperature of 1400 ^oC. From this viewpoint, it is quite important to understand the science and engineering and develop a fundamental understanding of HfO_2-based TBCs. This work is focused towards nanostructured HfO_2-based coatings, namely Y_2O_3-stabilized HfO_2 (YSH), Gd_2O_3-stabilized HfO_2 (GSH) and Y_2O_3-stabilized ZrO_2-HfO_2 (YSZH) for TBCs of advanced hydrogen turbines. HfO_2-Y_2O_3 and HfO_2-ZrO_2-Y_2O_3 targets were prepared and tested for TBC fabrication. Yttria stabilized hafnia (YSH) target was prepared using 92.5% HfO_2 and 7.5% Y_2O_3. The other specific compositions were prepared using a solid state reaction, cold-pressing and sintering. In addition, Gd_2O_3-HfO_2 compositions were also prepared. Coatings were grown on nickel-based super alloy, Inconel 738 and stainless steel. The effect of synthetic conditions and composition on the TBC coating structure and surface morphology was investigated in detail. A comprehensive understanding of the hafnia-based coatings' microstructure, mechanical behavior, thermo-chemical stability and thermal oxidation was developed. X-ray diffraction (XRD) and Electron microscopy analyses coupled with energy dispersive X-ray spectrometry (EDS) were used to gain a detailed understanding of crystal-structure, morphology, and stability of the coatings. Thermal conductivity of the YSH, YSZH and GSH compositions were evaluated. Laboratory experiments using accelerated test environments were be used to investigate the relative importance of various thermo-mechanical and thermo-chemical failure modes of TBCs. Effects of thermal stress cycling, oxidation degradation and their complex interactions on TBC failures were be evaluated using a syngas combustor rig. The results are presented and discussed.

Table of Contents

I. INTRODUCTION

Thermal barrier coatings (TBCs) are protective layers of low thermal conductivity ceramic refractory material whose functions are to protect the components from high temperature exposure. By making a barrier between hot gas environments the metallic parts, TBCs allow to increase the operating temperature which subsequently increases the overall efficiency of the turbines for power generation systems [1-5]. Ceramic materials for TBC applications have been, therefore, increasingly gaining importance since increasing the efficiency of gas turbine systems can be facilitated by elevating the operating temperature. The present state of art of the multicomponent TBC system consists of yttria stabilized zirconia (YSZ; 6-8% yttria) top coat, thermally grown oxide (Al_2O_3) and bond coat (typically NiCrAlY or NiCoCrAlY) [5, 6]. However, application of YSZ ceramic top coat is limited to 1200 ^oC due to a phase transformation after this temperature [7, 8]. The phase transformation of zirconia initiates cracks which ultimately lead to the failure of the TBC system [7, 8]. The limitation of zirconia based TBCs for surface temperature tolerance opens the door for research and development of novel TBCs which can withstand higher temperatures for utilization in advanced gas turbine technology.

Future generation gas turbine engines should tolerate fuel compositions ranging from natural gas to a broad range of syngas with high hydrogen contents which require TBCs with a surface temperature tolerance much higher than the current standard materials. The nanostructure of the TBC materials, in addition to composition, exhibits a great influence on many of the properties and performance of TBCs system [9-19]. Therefore nanostructured materials for TBC application have been receiving significant attention. Improved performance compared to the conventional material of same composition and possibilities for adopting the fundamental behavior that can benefit the engineering principles are the main driving factors. Because of the large volume fraction of internal interfaces, many important properties of nanostructured materials were found to be different from their conventional counterpart [12]. The most important physical and mechanical properties such as mechanical strength, indentation crack resistance, adhesion strength, spallation resistance, abrasive wear resistance and sliding wear resistance were found to be superior in nanostructured Al_2O_3-TiO_2 compared to the conventional bulk of the same material [10-12]. It has been demonstrated that nanostructured partially stabilized zirconia coating exhibits higher bond strength [13, 14-19, 20]. Amorphous materials are expected to have significantly lower thermal conductivity at room temperature than similar crystalline materials; however, the difference is not significant at temperatures more than the Debye temperature [16]. As the nanocrystalline materials exhibit grain boundary scattering as an extrinsic phonon-scattering phenomenon, they are expected to lower the thermal conductivity. Still it needs intrinsic evidence of these performances at elevated temperatures. A study of nano-crystalline stabilized zirconia ceramics reported that there was no significant effect of grain size on thermal conductivity [21], while some studies indicate that there was some extent of grain size effect on thermal conductivity for size below 30 nm [19]. However, the effect of nanocrystalline structure on thermal conductivity is less than that of Y content and oxygen vacancies in YSZ. The problem with the nanocrystalline material is that the

material starts to coarsen at long time operation [22]. Therefore, nanoporous materials that can resist coarsening of the porosity are of great interest for TBC materials. Nanostructured hafnia based TBCs are also associated with the reduction in weight of the TBCs which is a crucial factor for designing gas turbine rotating components. The focus of this project work is to engineer and develop a fundamental understanding of TBCs based on nanostructured HfO_2 coatings, namely Y_2O_3-stabilized HfO_2 (YSH), Gd_2O_3-stabilized HfO_2 (GSH) and Y_2O_3-stabilized ZrO_2-HfO_2 (YSHZ) for advanced hydrogen turbines. It has been demonstrated that the yttria stabilized hafnia (YSH) reveals a great potential to be considered for TBCs. Because of its suitable phase stability, lower thermal conductivity in wide range of temperature and excellent radiation stability, the Y-stabilized Hafnia material systems deserves attention to engineer the TBCs with higher temperature tolerance.

The approach is to systematically vary the growth conditions and target/ingot materials to study their influence on the coatings' phase, microstructure, mechanical, thermal, chemical properties, and performance. The qualitative and quantitative models for failure mechanisms, life time and performance of the nanostructured YSH, GSH, and YSZH ceramic TBCs have been developed from all these studies. The models will be used to predict pathways to further improve the coatings microstructure (at the reduced nano-dimensionality), properties and ultimately the performance. The central theme of the microstructure evaluation and various characterizations is to provide feedback to fabrications so as produce materials with superior stability, high temperature tolerance, thermal durability and reliable sensitivity.

The specific objectives are: (a) Development of Y_2O_3-HfO_2, Gd_2O_3- HfO_2 and Y_2O_3-HfO_2-ZrO_2 thermal barrier coatings on various substrates (IN 738, SS403, Alumina & Si) varying the composition of coatings and growth temperatures. (b) Investigating physical and mechanical properties of coatings and optimization of materials processing to yield superior coating characteristics. (c) Demonstrate the high temperature stability of crystal structure with columnar interface morphology. (d) Detailed information on the thermo-mechanical and thermochemical properties of the yttria-stabilized hafnia (YSH), gadolinia stabilized hafnia (GSH) and yttria stabilized zirconia-hafnia(YSHZ) coatings. (e) Investigation of durability in hot gas environment.

HfO_2-Y_2O_3, HfO_2-Gd_2O_3 and HfO_2-ZrO_2-Y_2O_3 targets were prepared and tested for TBC fabrication. Yttria stabilized hafnia (YSH) target with composition 92.5% HfO_2 and 7.5% Y_2O_3. The other specific compositions were prepared using a solid state reaction, cold-pressing and sintering. Coatings were grown on nickel-based super alloy, Inconel 738, Alumina and stainless steel. The effect of synthetic conditions and composition on the TBC coating structure and surface morphology was investigated in detail. A comprehensive understanding of the hafnia-based coatings' microstructure was derived. Detail understanding of structural, morphological, physico-chemical and thermo mechanical properties and performance in hot gas environment was made by characterizing, testing and exposing the coatings to the hot gas using laboratory scale combustor rig.

II. MATERIALS AND METHODS

Target Preparation

YSH, YSHZ and GSH targets (5.0 cm diameter and 0.3 cm thickness) were used to fabricate the hafnia based coatings. YSH, YSHZ and GSH targets of mixed compositions were made with mixed proportions of HfO_2 and ZrO_2 stabilized by either Y_2O_3 or Gd_2O_3. The composition of the target material was varied by varying the ratio of HfO_2 and ZrO_2 while keeping the Y_2O_3 stabilizer content constant at 7.5 mol% in YSHZ coatings. The ratio of HfO_2 and ZrO_2 was varied in the proportions of 4:1, 2:1, 1:1, 1:2 and 1:4. The composition was then stabilized with yttria at 7.5 mol% of the total amount of material including yttria. The composition is summarized in Table 1.

Table 1: Composition of the target materials

Target	**Molar ratio of HfO_2 to ZrO_2**	**Amount of Y_2O_3**
YSH	1:0	7.5%
YSHZ-1	4:1	7.5%
YSHZ-2	2:1	7.5%
YSHZ-3	1:2	7.5%
YSHZ-4	1:4	7.5%
YSHZ-5	1:1	7.5%

Stoichiometric amounts of HfO_2, ZrO_2 and Y_2O_3 powders were mixed thoroughly along with small amount of poly vinyl alcohol (PVA) binder. The mixture was then subjected to very high pressure compression to make a 5 cm pellet in a die at a pressure of 24000 lbs for 30 minutes followed by sintering at 1050 ^{o}C for 24 hrs. The target of 5 cm diameter and 0.3 cm thickness thus obtained was fixed to a 5 cm Cu backing plate at the bottom of the pellet using an epoxy glue to get the stable target ready to be used for TBC deposition. Additionally, pellets of 0.78 cm diameter were also prepared following the same procedure. These small diameter pellets were prepared in order to investigate the properties of bulk materials with the same composition as that in dense coatings. The sequential steps for the target fabrication are shown in Figure 1. Target for GSH coatings were prepared (Table 2) by varying the proportion of Gd_2O_3 in the range of 0-38 mol%, rest balanced for HfO_2 following the same procedure for YSH and YSHZ.

Table 2: Composition of Gd_2O_3 based hafnia ceramics

Gd_2O_3 : 4 mol%
Gd_2O_3 : 8 mol%
Gd_2O_3 : 12 mol%
Gd_2O_3 : 20 mol%
Gd_2O_3 : 38 mol%
} Balance HfO_2

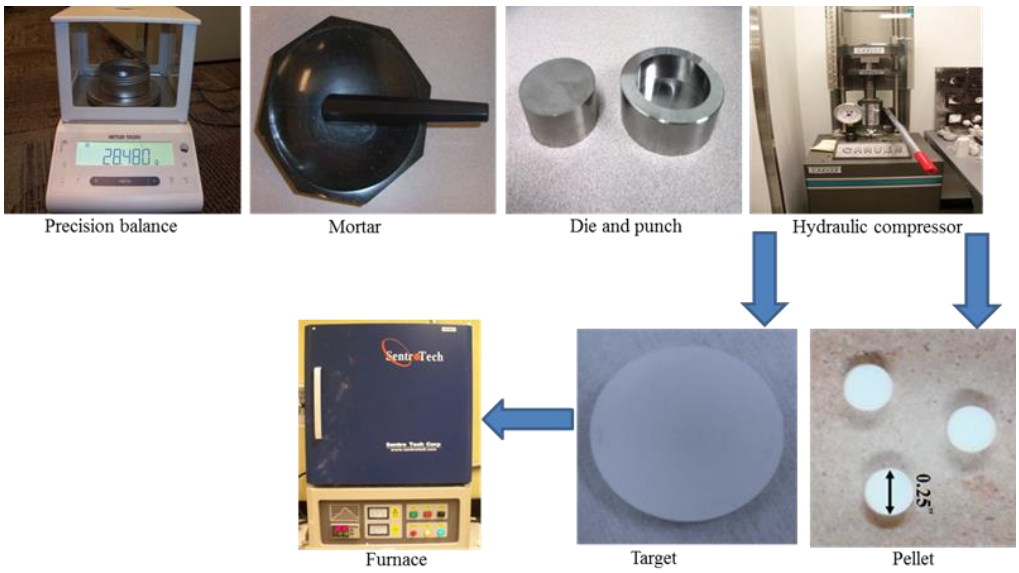

Figure 1: Sequential steps for the fabrication of YSHZ targets

Coatings' Deposition

Two physical vapor deposition methods namely sputtering and electron beam physical vapor deposition (EBPVD) were employed in this research to fabricate the coatings. The YSH/YSHZ/GSH target was placed on a 5 cm sputter gun, which was correspondingly placed at a distance of 8 cm from the substrate. A high vacuum was produced in order to create the plasma. When the level of $3x10^{-6}$ torr was achieved, a sputtering power of 30 W was initially applied to the target while introducing high purity argon (Ar) into the chamber causing plasma ignition. Once ignited, the power was increased to 100 W to deposit the coatings. The flow of the Ar was controlled using MKS mass flow meter. Before each deposition, the YSH-target was pre-sputtered for 10 minutes using Ar with the shutter above the gun closed. A variety of operating parameters were used to optimize the deposition conditions. The substrates were heated by halogen lamps and the desired temperature was controlled by Athena X25 controller. Various deposition durations were maintained to grow the TBC with different thicknesses. Various gas (Ar) velocity were used to optimize the plasma flow for forming uniform thin film on substrates. The whole deposition was carried out at a constant vacuum level of $4.10x10^{-3}$ torr.

In EBPVD system, the evaporating material was used in the form of ingots. A graphite crucible filled with the evaporating materials (YSH or YSHZ) was placed in EB gun system. The gun is designed in such a way that there are four crucibles which can be moved mechanically to change the materials for evaporation. The substrates to be coated were placed at a distance of 20 cm above the evaporating materials placed in the crucible. The chamber was then evacuated to a level of 10^{-6} torr. After getting the desired vacuum, the current was increased slowly up to 280 mA using 8.16 kV. Before each deposition, the pre-evaporation was carried out for 10 minutes keeping shutter closed above the gun and then the deposition was carried out at 10^{-5} torr. After every deposition, the samples

were subjected to a heat treatment at 600 ^{0}C for 6 hrs. in order to enhance the proper crystal growth. The bond coat of Nickel aluminide alloy (NiCoCrAlY) was grown on substrates using plasma pray. A 100 µm thick layer of bond coat was deposited on two types of substrates SS-403 and Inconel-738. A heat treatment was performed at 600 ^{o}C for 6 hrs just after the deposition in order to allow the substrates to react with the bond coat properly.

III. RESULTS AND ANALYSIS

Crystallography

The XRD patterns of YSH coatings grown on SS-403 and Inconel-738 are shown as a function of growth temperature (T_s) in Figure 2. The XRD patterns of YSH coatings exhibit the peaks corresponding to cubic structure of HfO_2. It is evident that the effect of growth temperature is not very significant on the phase except with an increase in the average grain size. The peak at ~30.28° (Fig. 2a) corresponds to the diffraction from (111) planes. This peak is rather broad for coatings grown at T_s=RT indicating the presence of nano-crystalline particles embedded in an amorphous matrix. It can be noted from the XRD patterns (Fig. 2a) that the (1 1 1) peak becomes sharper with increasing growth temperature. A decrease in the full-width at half-maximum (FWHM) associated with an intensity increase of the peak can be noted in the XRD data (Fig. 2b). This observation clearly indicates that the crystallinity of the coating is improved with increasing growth temperature. This is also indicative of an increase in the average crystallite-size and preferred orientation of the film along (111). Monoclinic and tetragonal phases consist of several shorter Hf-O bond lengths (2.0–2.1 Å) compared to cubic HfO_2 (2.37 Å) [23]. As a consequence, the strain energy because of the size mismatch becomes significant in monoclinic and tetragonal phases. On the other hand, the distortion is quite less in cubic phase with the oversized Y^{+3} doping, which makes cubic HfO_2 stable even at low temperature. Furthermore, the structural relaxation plays another role in the stabilization of cubic phase of HfO_2 by Y_2O_3 dopant [23].

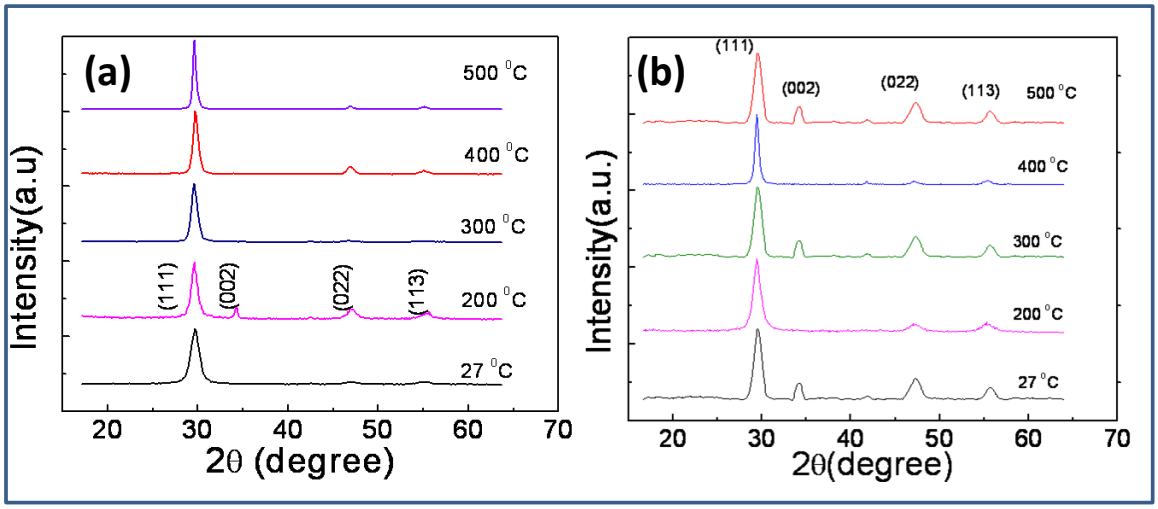

Figure 2: The XRD patterns of YSH coatings on SS-403 grown (a) and Inconel-738 (b).

It is evident from Figure 2b that the width of the peak corresponding to (111) planes decreases with the increasing temperature (to 400 ^{o}C) when YSH coatings are grown on Inconel-738. As mentioned above, the decrease in peak width is associated with the increase in crystallite size and the extent of crystallization. However, the peaks are rather broad for the sample grown at 500 ^{o}C compared to other growth temperatures. This might be because of the fact that Inconel-738 super alloy consists of several elements which possesses different thermal expansion coefficient compared to one another. At 500 ^{o}C, all these elements get enough thermal energy for lattice expansion but slightly in different magnitude. Therefore, when YSH is deposited on the super alloy at higher temperature, the peak width increases because of the wide range of the inter planner spacing while maintaining the cubic crystal structure.

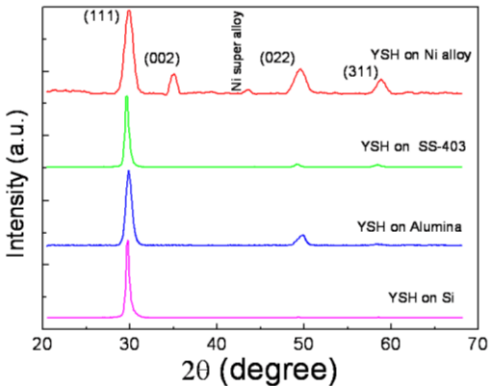

Figure 3: XRD patterns of YSH coatings on various substrates

The effect of substrate materials on the crystal structure of YSH coatings grown at 500 ^{o}C is shown in Figure 3. It is evident (Fig. 3) that the substrate materials don't show very significant effect on crystal structure of YSH coatings. YSH crystallizes in cubic structure on all of these four substrates.

The XRD patterns of the YSHZ coatings grown on alumina and stainless steel substrates are shown in Figures 4a and 4b. It is evident from the XRD patterns that the coatings are crystallized in the cubic structure of HfO_2. All of the compositions of hafnia and zirconia coatings on all the substrates showed the similar crystal structure (Figs. 4a and 4b). The effect of temperature is not significant although some peak sharpening can be seen with increasing temperature. Another important feature that can be noted in XRD data is that the patterns of YSHZ coatings are very similar to the cubic structure of YSH coatings (Figs. 3 and 4). This observation indicates that the stabilization of cubic hafnia phase is mainly due to the presence of yttria stabilizer. The phase stabilization is independent of the ratio of HfO_2 and ZrO_2 and the type of substrates.

It has already been established that ZrO_2 can be stabilized in cubic phase by selectively doping with Y_2O_3, CeO_2 and MgO [24]. Since Y_2O_3 exhibits cubic-centered Tl_2O_3-type structure it is possible that yttria can stabilize the hafnia in cubic structure [25-27]. Therefore, cubic-phase stabilization in Y_2O_3–HfO_2–ZrO_2 coatings is a result of oxygen vacancy creation similar to the case of ZrO_2. The Y^{+3} ions having radii (0.96 Å) larger than that of Hf^{+4}/Zr^{+4} imparts lattice distortion and enforce the elongation of bond with oxygen in close propinquity. Therefore, the stabilization of YSHZ is similar to that in YSH as described above. As seen in the XRD data (Figs. 4a and 4b), the cubic structure of YSHZ coatings is retained down to room temperature like YSH.

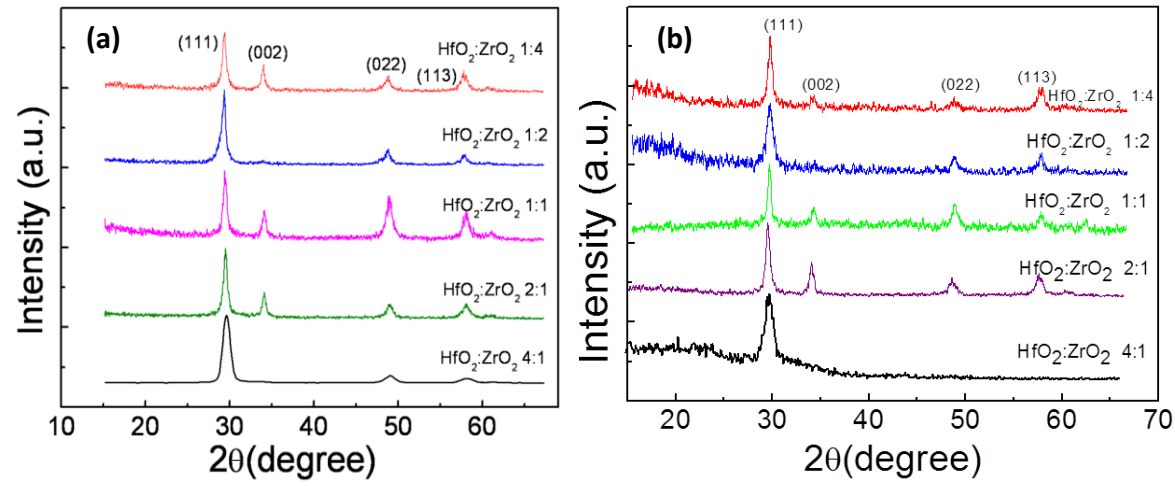

Figure 4: XRD curves of YSHZ coatings on alumina (a) and SS-403 (b)

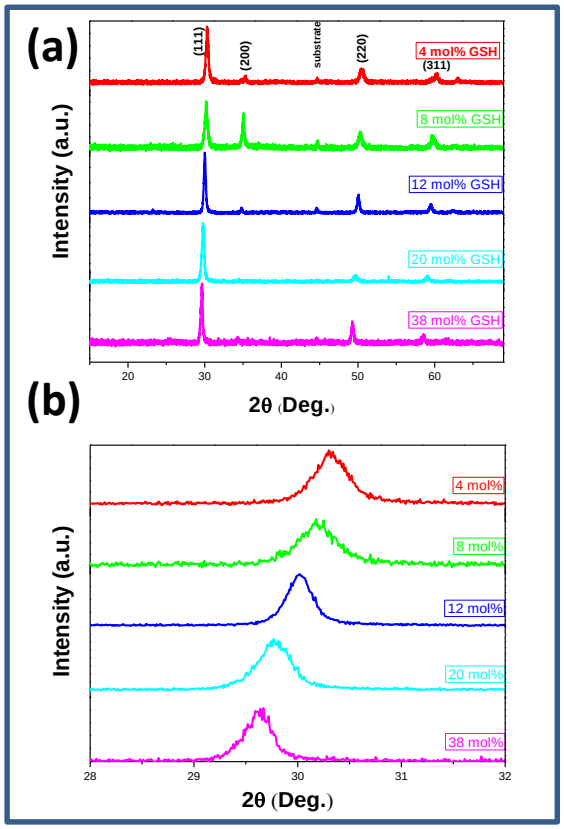

Figure 5: (a) XRD patterns of GSH; (b) Expanded, high resolution scan of the (111) peak of the Gd_2O_3-HfO_2 coatings.

XRD patterns of GSH nanocrystalline coatings are shown in Figure 5. The patetrns shown are as a function of the Gd_2O_3 content in the coatings. A shift in the most intense (111) peak with increasing Gd_2O_3 is evident from the XRD patterns (Fig. 5a). The peak shifts to lower diffraction angle. Indexing of the patterns indicate that the coatings exhibit the crystal structure of the cubic hafnia phase. The cubic HfO_2 phase formation can be attributed to the effect of Gd_2O_3 acting as a stabilizer. However, the effect of Gd_2O_3 as a stabilizer resulting in the cubic HfO_2 phase is effective up to a concentration of 12 mol%, at which point the formation of pyrochlore $Gd_2Hf_2O_7$ occurs. The grains are highly oriented along the (111) direction. The (111) peak position shifts from $2\theta=30.32^0$ to $2\theta=29.62^0$ with increasing Gd_2O_3 content from 4 to 38 mol% (Fig. 5b). This is an indication of the expansion of the lattice by the expansion of the interplanar spacing (d) with Gd_2O_3 concentration.

The lattice parameter dependence on the composition of YSZH and GSH coatings is shown in Figure 6. The lattice parameter of the YSH coatings calculated from XRD data

was found to be ~0.52 nm, which is close to the reported value of cubic hafnia. Lattice parameter variation is due to the changes in lattice-strain and crystallite size in nanocrystalline YSH. The lattice constant obtained for YSH coatings (Fig. 6a) is larger as compared to that of pure HfO_2 (5.09Å). (1) This lattice expansion in YSH compared to pure HfO_2 is caused by the addition of 7.5% Y_2O_3 and can be understood as follows. The ionic radii of Y^{+3} (0.96 Å) is larger than that of Hf $^{+4}$ which introduces lattice distortion and enforce the elongation of bond with oxygen in close proximity. However, there is an increasing trend of the lattice constant with increasing ZrO_2 in YSHZ coatings. The lattice constant variation with ZrO_2 content of the YSZH coatings is shown in Figure 6a. Enhancement in the lattice parameter with a progressive increase in the ZrO_2 concentration is due to the interactions of Zr^{+4} and Hf^{+4} ions. While the charge and radius of the zirconium and hafnium ions are more or less similar, the lattice parameter of cubic Y_2O_3–ZrO_2–HfO_2 coatings seems to be influenced by the ZrO_2 addition since the ionic radius of Zr^{+4} is slightly higher than that of Hf^{+4} (10). The physical mechanisms involved in the lattice parameter variation of Y_2O_3–ZrO_2–HfO_2 coatings can be understood as follows. The lattice parameter enhancement, in general, in Y_2O_3–HfO_2–ZrO_2 coatings compared to pure HfO_2 is caused by the addition of 7.5% Y_2O_3 and associated lattice distortion and elongation of bonds. The lattice distortion increases when the number of Zr^{+4} ions is more than the Hf^{+4} ions in the matrix leading to overall lattice expansion to accommodate the Y^{+3}, Zr^{+4} and Hf^{+4} ions.

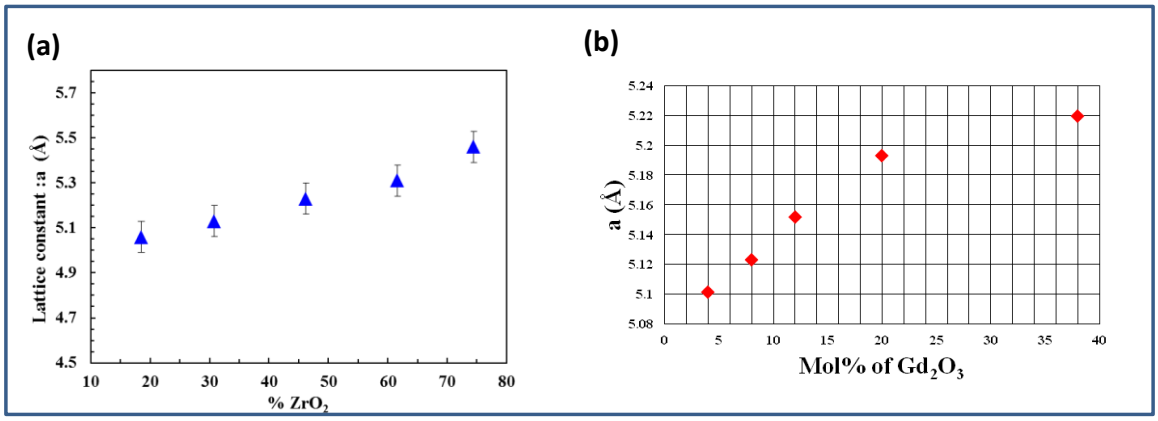

Figure 6: The variation of lattice parameter with: (a) ZrO_2 content in YSHZ coatings; (b) Gd_2O_3 content in GSH coatings

The lattice constant of the GSH coatings was calculated from the d value of the most intense (111) peak. The peak positions were obtained after fitting the peak with a Gaussian function. The error in measuring the (111) peak position (2θ) peak was ~0.0015^0. The lattice constant variation with Gd_2O_3 composition is shown in Fig. 6b. It is obvious from the plot that the lattice constant of the GSH coatings increases from 5.101 Å to 5.219 Å as the Gd_2O_3 concentration increases from 4 to 38 mol%.

The XRD results and the physical mechanisms involved in the lattice parameter variation of Gd_2O_3-HfO_2 coatings can be understood as follows. The lattice expansion and cubic-phase stabilization in Gd_2O_3-HfO_2 coatings for lower concentrations of Gd is a result of

oxygen vacancy creation. The Gd^{+3} ions having radii (0.94 Å) larger than that of Hf^{+4} imparts lattice distortion and enforces elongation of the bond with oxygen. The lattice parameter enhancement in Gd_2O_3-HfO_2 coatings compared to pure HfO_2 is, therefore, due to the Gd^{3+} ions and associated lattice distortion. The observed further increase in lattice parameter with progressive increase of Gd_2O_3 can be attributed to higher concentration of Gd^{3+} ions with sizes larger than that of Hf^{4+}. The lattice distortion increases when the number of Gd^{4+} ions is more than the Hf^{4+} ions in the matrix leading to overall lattice expansion to accommodate the Gd^{3+} and Hf^{4+} ions.

Surface and Interface Morphology

The SEM images indicating the surface morphology of the YSH coatings are shown in Figure 7. The morphology of the coatings is characterized by thin, elongated triangular network of grains connected together to form the dense surface structure. Based on the XRD and SEM data, it seems that a temperature of 300 ^{o}C is the critical temperature to promote ordered, oriented growth of YSH nanocrystalline coatings. At this temperature, the grains are fully grown and uniformly distributed across the sample surfaces. Triangular shaped grains, which are oriented in a specific morphology as seen in the SEM micrographs, provides the characteristic dense structure of the YSH coatings. For thick YSH coatings, Matsumoto et al. have reported that the morphology is characterized by the presence of triangular shaped grains on the surface [6]. In the present case, it seems that the signature of that characteristic is present although the coating thickness and size are significantly lower. Thus, the crystal structure and well defined grain size with increasing temperature can be attributed to the effect of temperature, which increases the mobility of the surface species to account for the observed results shown in Figures 7 and 8. When the samples are grown as thick coating, the grains tend to grow in large size after complete crystallization. The grains are still triangular shape with tiny pores all around the sample which is similar to that reported by Matsumoto et al. [6]. The morphology of thick samples grown on SS-403 and inconel-738 with bond coat with and without bond coat are shown in Figure 8.

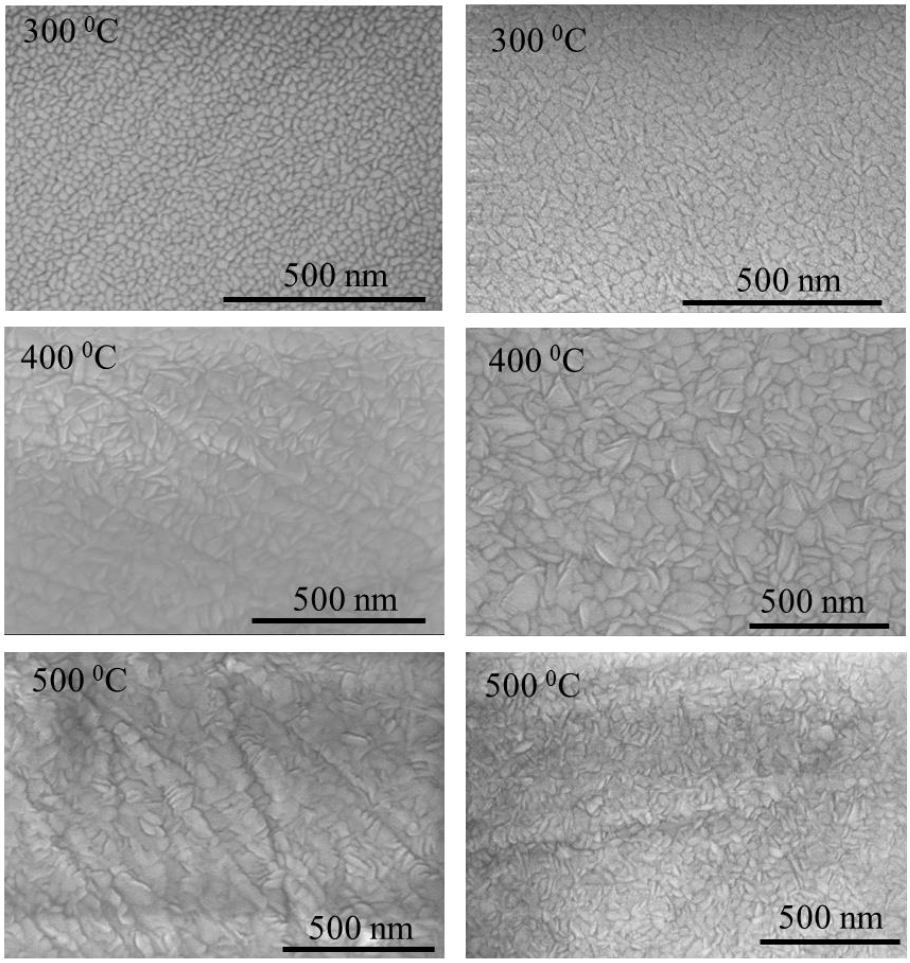

a) **b)**

Figure 7: SEM images of YSH coatings on Inconel-738 (a) and SS-403 (b) substrates.

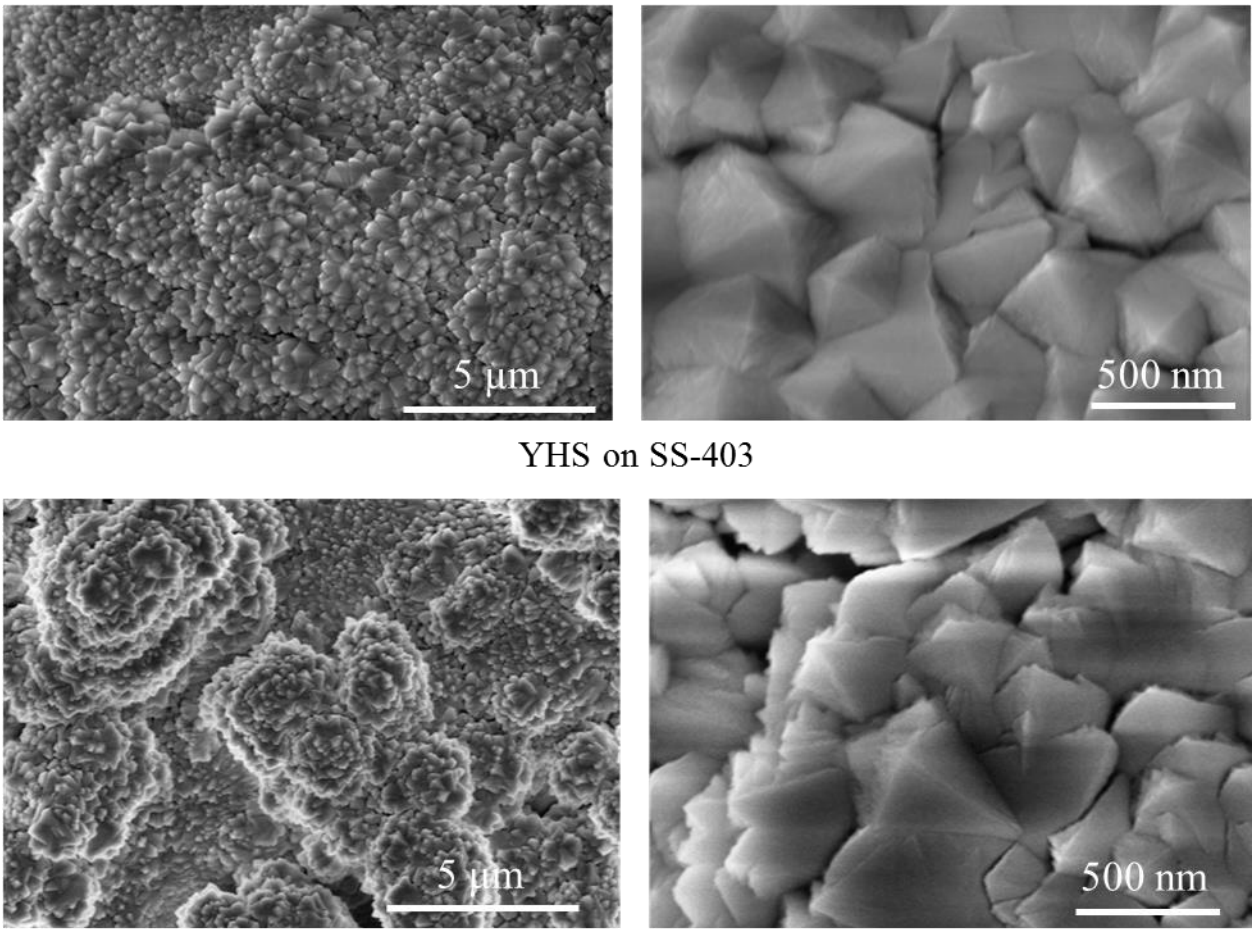

Figure 8: Surface morphology of YSH coatings grown on SS-403 and Inconel-738 with bond coat

The surface morphology of the representative YSZH coatings are shown in Figures 9, 10, and 11. High magnification SEM images show the morphology consisting of very well and densely oriented grains in all of the YSHZ coatings grown on SS-403 at 500 ^{o}C (Figure 9). However, YSHZ coatings grown at room temperature exhibit the grains, which are smaller in size and not very clear even at high magnifications (Figure 10). The morphology looks like a dense cauliflower structure when grown on Inconel-738 (Figure 10). It is evident that the ZrO_2 addition induces changes in the morphology of the coatings. Based on the results obtained and results reported for EB-PVD grown coatings, it appears that thin, elongated triangular shape morphology is the characteristic of the yttria–stabilized hafnia. However, as it is seen in XRD, the deviation of such morphology with progressive addition of zirconia is believed to be due to the distortion as a result of Zr^{+4} ions replacing the Hf^{+4} ions. However when YSHZ is grown as thick coating (as shown in Figure 9) the grains tend to grow bigger and arrange in triangular shape and well developed crystallites similar to YSH coatings as shown in Figure 9. Therefore, it is evident that the influence of ZrO_2 addition on the surface morphology of YSHZ coatings

is not significant when the coating is thick enough (~3 μm) to achieve the complete crystallization.

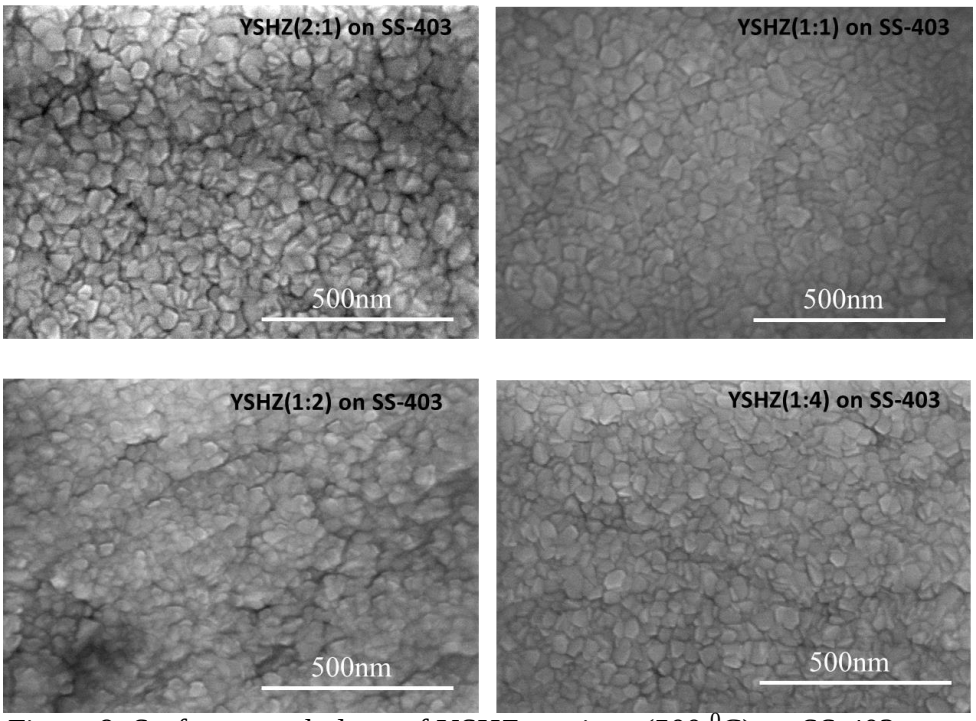

Figure 9: Surface morphology of YSHZ coatings (500 ^{0}C) on SS-403

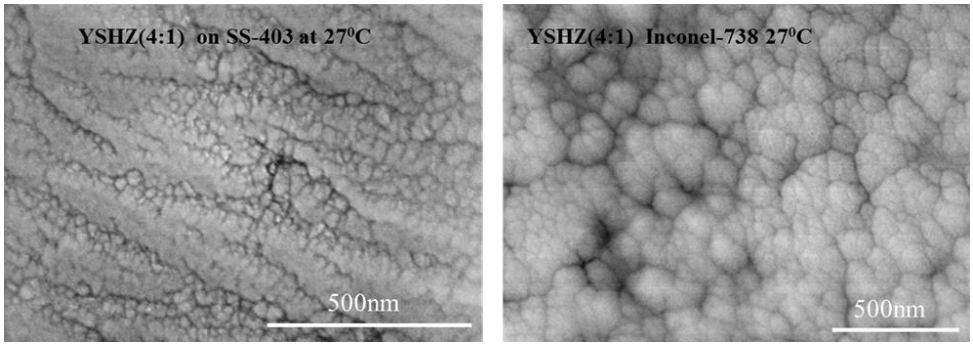

Figure 10: Surface morphology of YSHZ coatings

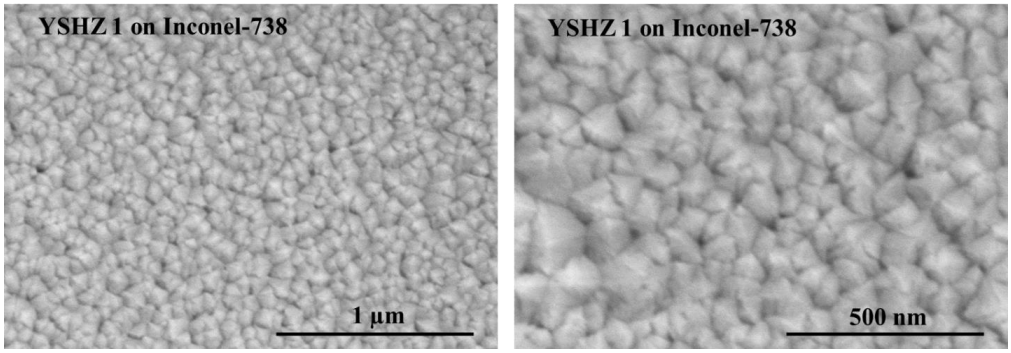

Figure 11**:** Surface morphology of YSHZ coatings (~3μm)

The SEM images of GSH coatings are shown in Figure 12. The surface morphology is remarkably different at various substrate temperatures. The GSH coatings grown at RT are not fully amorphous as indicated by the SEM images. But the degree of crystallinity is less at RT. This result is in agreement with the XRD analysis. Coatings grown at 500 ^{0}C are highly crystalline for all the compositions. The grains are nanostructured and triangular in shape at a substrate temperature of 500 °C.

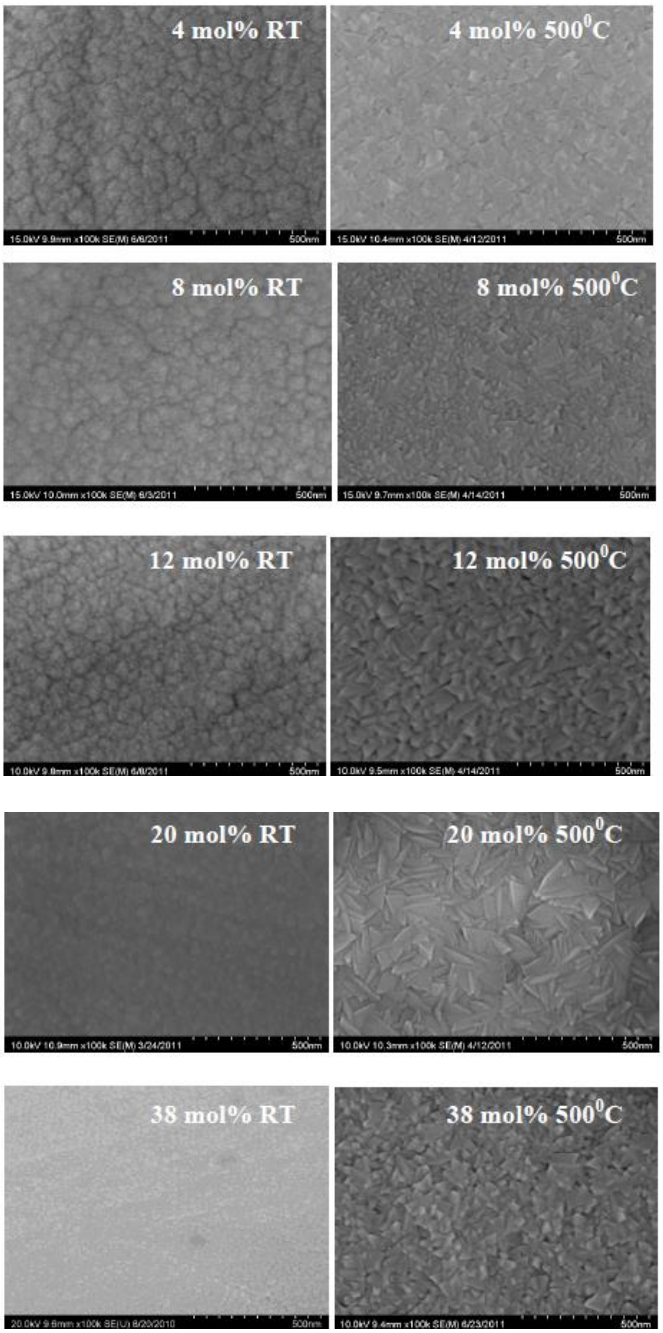

Figure 12: SEM images of the different compositions GSH coatings.

All the YSHZ and YSH coatings exhibit the columnar structure that is typically observed in these ceramic coatings. The columnar growth of the coatings is generally favorable for higher mechanical strength. A representative of the coatings interface structure exhibiting the columnar growth is shown in Figure 13. Such structure was retained for several microns.

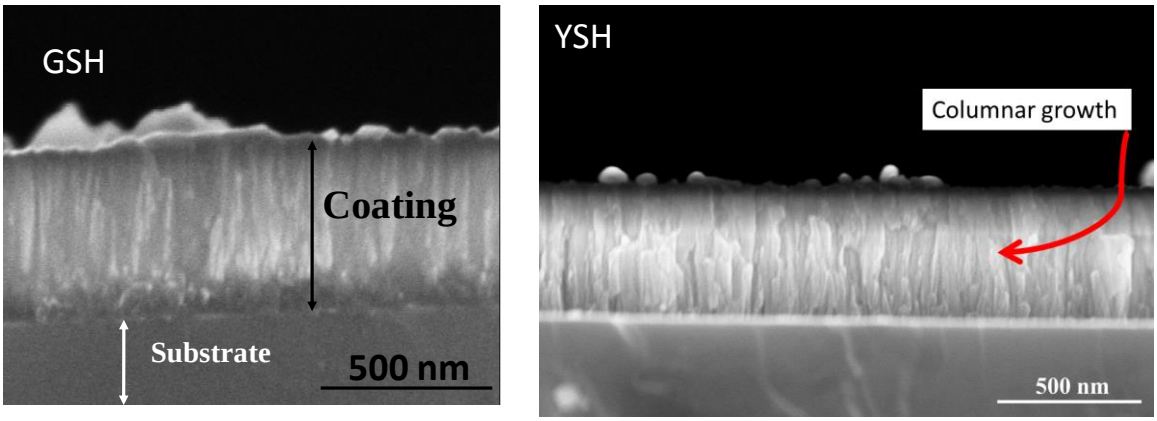

Figure 13: Typical columnar growth of the coatings

The average grain size variation, determined from XRD data and SEM imaging analysis, with growth temperature is shown in Figure 14. It is evident that the grain size increases with increasing growth temperature which can be explained as follows.

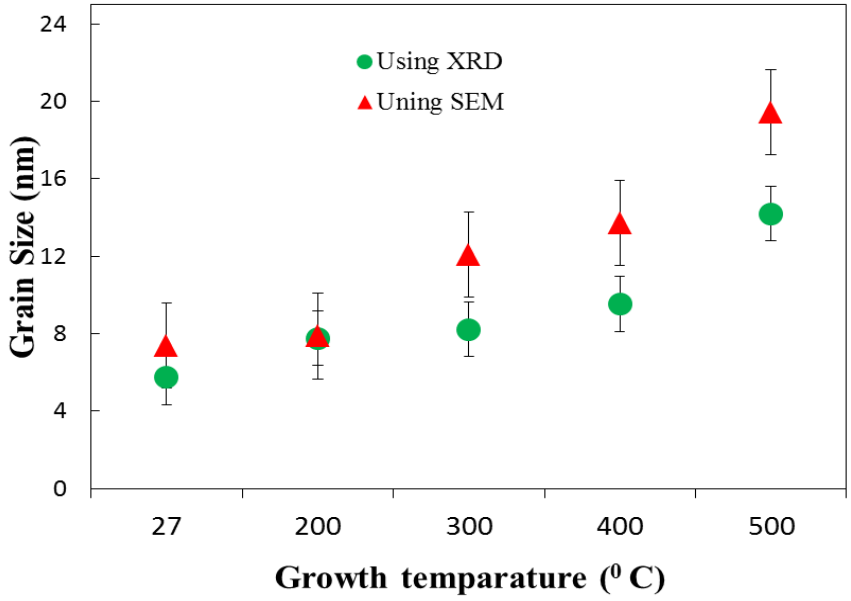

Figure 14: The variation of average grain size of YSH coatings with growth temperature

Composition

It is important to verify that the composition of the coatings is retained similar to the target and compositional stability as a function of growth temperature. The EDS spectra of the YSH and YSHZ coatings are shown in Figures 15 and 16 respectively. The EDS curve indicates the X-rays emitted from various elements. The peaks corresponding to Y, Hf, and O atoms present in the sample are as labeled (Figures 15 and 16). The respective energy positions and the specific X-ray lines from various elements are also indicated in those figures. Intensity of the peaks corresponds to the composition of each element as labeled in Figures 15 and 16. The absence of any other peaks except from Y, Hf, and O indicates the YSH and YSHZ coatings without any elemental impurities incorporated during chemical processing and/or post-fabrication handling. It was found from the EDS analysis that the same composition of the target used for the deposition retains in the coating when grown using magnetron sputtering indicating the effective transfer of the stoichiometry during deposition of the coating.

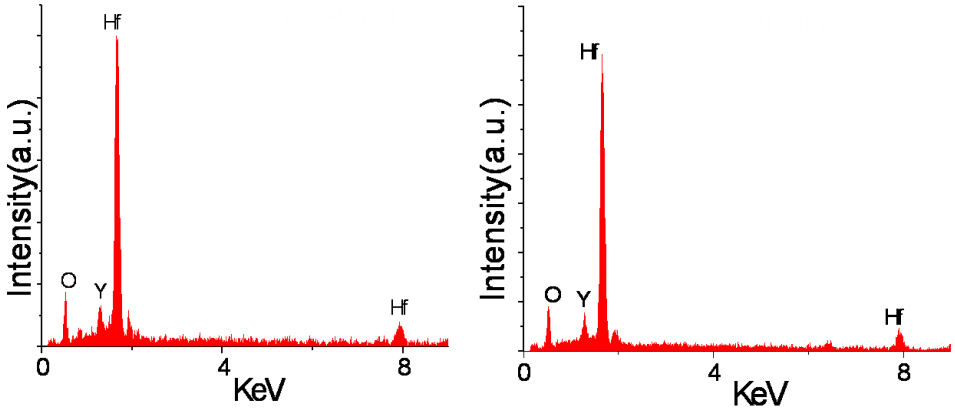

Figure 15: EDS spectrum of YSH coatings grown at 500 ^{0}C. The X-ray peaks due to Y, Hf and O atoms and their respective positions are as indicated for the EDS curve.

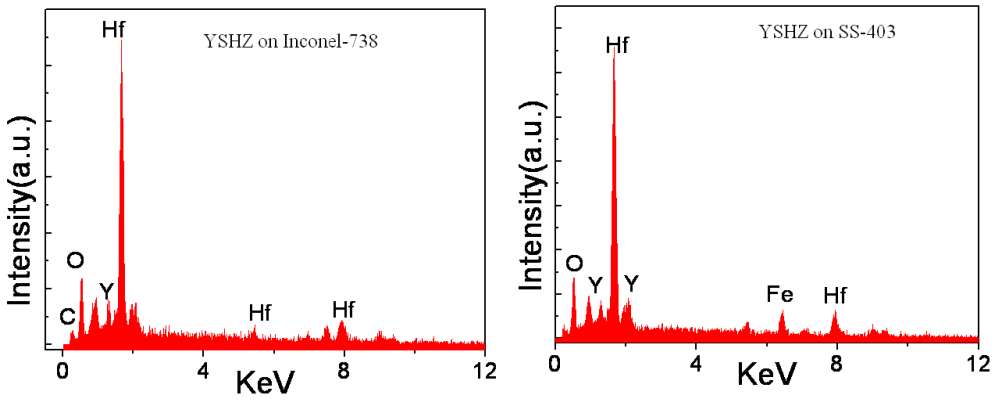

Figure 16: EDS spectrum of representative YSHZ coatings grown at 500 ^{0}C.

The EDS spectra of GSH coatings as a function of Gd_2O_3 concentration are presented in Figure 17. The peaks corresponding to Gd, Hf, and O atoms present in the sample are as labeled (Figure 17). The peak of Fe appears from the stainless steel substrate. The

absence of any other peaks except from Gd, Hf, and O indicates the high quality GSH coatings without any elemental impurities incorporated during deposition. It is obvious from the EDS spectra that the peak intensity of Gd and O is increasing and the intensity of Hf peak is decreasing with the increase of Gd_2O_3, as it is expected. The elemental composition is presented in Table 2. It can be seen from the table that Gd concentration increases from 4.8 wt% to 30.13 wt% in the GSH coatings. The corresponding Hf concentration decreases from 89.5 wt% to 62.08 wt% as the Gd2O3 content is increased from 4 to 38 mol%. This observation indicates that the composition of deposited coating is very close to the sputtering target composition. So the deposition was very close to stoichiometry.

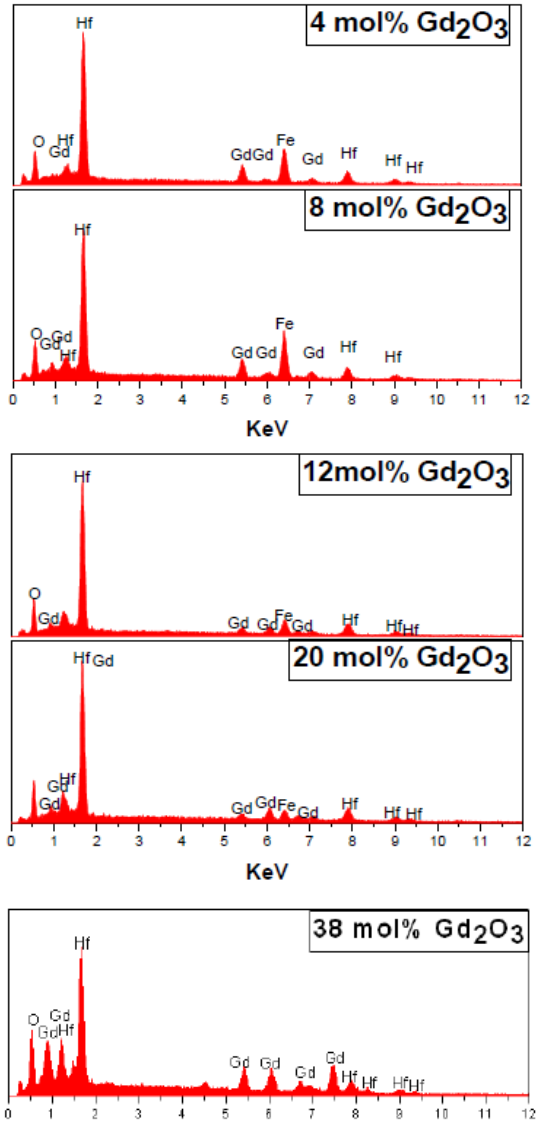

Figure 17: EDS spectra of GSH coatings grown at 500 ^{o}C on SS 403 substrate at various Gd_2O_3 concentrations. The peaks of Gd, Hf and O are labeled.

Table 2: Elemental composition of the GSH coatings.

Composition		Elements			Total
		O	Gd	Hf	
4 mol% Gd_2O_3	Wt%	5.70	4.80	89.5	100
	At%	40.41	3.44	56.15	
8 mol% Gd_2O_3	Wt%	6.27	10.08	83.65	
	At%	42.4	6.93	50.67	
12 mol% Gd_2O_3	Wt%	5.32	13.31	81.37	
	At%	38.1	9.69	52.3	
20 mol% Gd_2O_3	Wt%	5.52	17.69	76.79	
	At%	38.87	12.67	48.46	
38 mol% Gd_2O_3	Wt%	7.79	30.13	62.08	
	At%	47.43	18.67	33.9	

The distribution of Gd and Hf atoms on a particular surface area of the deposited GSH coatings of different compositions were investigated by performing mapping using EDS. Mapping images of GSH coatings indicated that the Gd concentration is increasing and Hf concentration is decreasing with the increase of Gd_2O_3 content as it is expected and the Gd and Hf atoms are evenly distributed on this particular surface area.

Thermal Conductivity

Thermal conductivity of YSH coatings was evaluated by both photo-acoustic (PA) and thermal diffusivity measurements. According to the thermal diffusion model (Rosencwaig–Gersho theory) [28], for an optically opaque sample, the expression for PA signal is:

$$\delta P = \frac{\gamma P_0 I_0 (\alpha_g \alpha_s)^{\frac{1}{2}}}{2\pi l_g T_0 k_g f \sinh(l_s \sigma_s)} \exp\left[j\left(\omega t - \frac{\pi}{2}\right)\right] \quad (1)$$

where γ is the air specific heat ratio, P_0, the ambient pressure, T_0, the ambient temperature, I_0, the absorbed light intensity and $\omega = 2\pi f$, where f is the modulation

frequency and l_i, k_i and α_s are the length, thermal conductivity and the thermal diffusivity respectively. Here the subscript i (= s, g) denotes sample (s) and gas (g) medium. $\sigma_i = (1 + j)a_i$ is the complex thermal diffusion coefficient of the material where $a_i = (\omega/2\alpha_s)^{1/2}$. If the sample is thermally thick then Eq. (1) reduces to,

$$\delta P \approx \frac{\gamma P_0 I_0 (\alpha_g \alpha_s)^{\frac{1}{2}} \exp -l_s \left(\frac{\pi f}{\alpha_s}\right)^{\frac{1}{2}} / f}{\pi l_g T_0 k_s} X \exp\left[j\left(\omega t - \frac{\pi}{2} - l_s \alpha_s\right)\right] \quad (2)$$

where l_s is the thickness of the sample. From Eq. (2), amplitude varies as:

$$\left(\frac{1}{f}\right) \exp\left[l_s \left(\frac{\pi f}{\alpha_s}\right)^{\frac{1}{2}}\right] \quad (3)$$

the phase varies as

$$-l_s \left(\frac{\pi f}{\alpha_s}\right)^{\frac{1}{2}} \quad (4)$$

Hence, the thermal diffusivity can be measured either from amplitude data or from phase data. The phase shift as a function of the modulation frequency for the YSH coatings is shown in Figure 18. The thermal conductivity of YSH coatings are found within the range from 0.89 ± 0.03 to 1.3 ± 0.04 W/m-K. Thermal conductivity of YSH coatings is shown in Figure 18. The two important observations that can be derived from thermal conductivity measurements of YSH coatings are as follows. The thermal conductivity of YSH coatings, in general, is lower than that of pure hafnia or bulk YSH is the first. The thermal conductivity slightly increases with increasing growth temperature is the later. The later behavior can be attributed to the increasing grain size with increasing growth temperature. Thermal diffusion through lattice vibrations in a solid can be affected by: (a) phonon–phonon interactions, (b) imperfections, and (c) grain boundary scattering. The effective grain boundary decreases with increasing grain size leading to a decrease in phonon scattering and, hence, resulting in the observed increase in thermal conductivity. Effective reduction in the thermal conductivity of the YSH coatings grown at RT can be attributed to an amorphous structure, where there exist only smaller particles occasionally. The thermal conductivity increase with increasing grain size has been reported for YSZ [19, 29]. On the other hand, the observed thermal conductivity decrease in yttria stabilized hafnia can be attributed to the addition of yttria to hafnia. Furthermore, thermal conductivity of YSH is much lower than that of pure hafnia. The reason for YSH materials exhibiting lower thermal conductivity than pure hafnia is the introduction of oxygen vacancies. These are structural vacancies in the hafnia crystals due to charge compensation of Y^{+3} ions substituting for Hf^{+4} ions. As a result, phonon scattering from the vacancies decreases effective thermal transport.

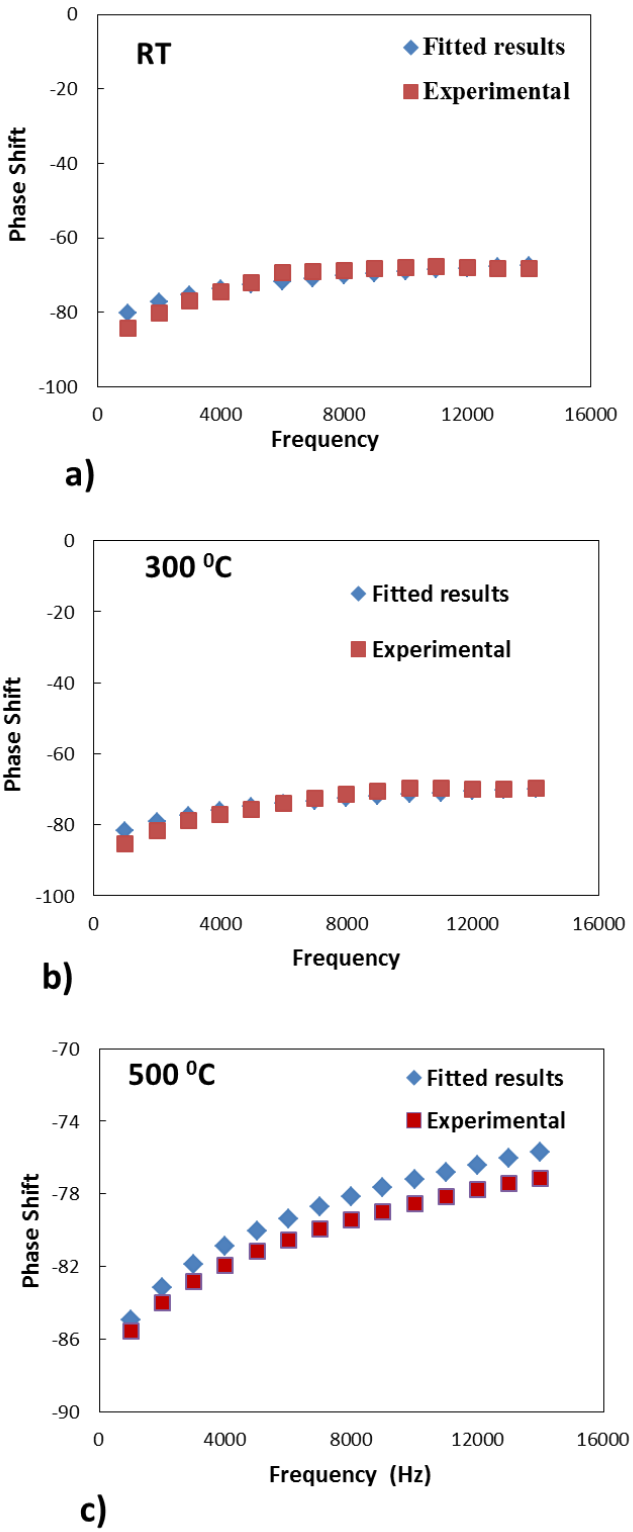

Figure 18: Phase shift with respect to modulation frequency for YSH grown at RT (a), 300 ^{0}C (b) and 500 ^{0}C (c).

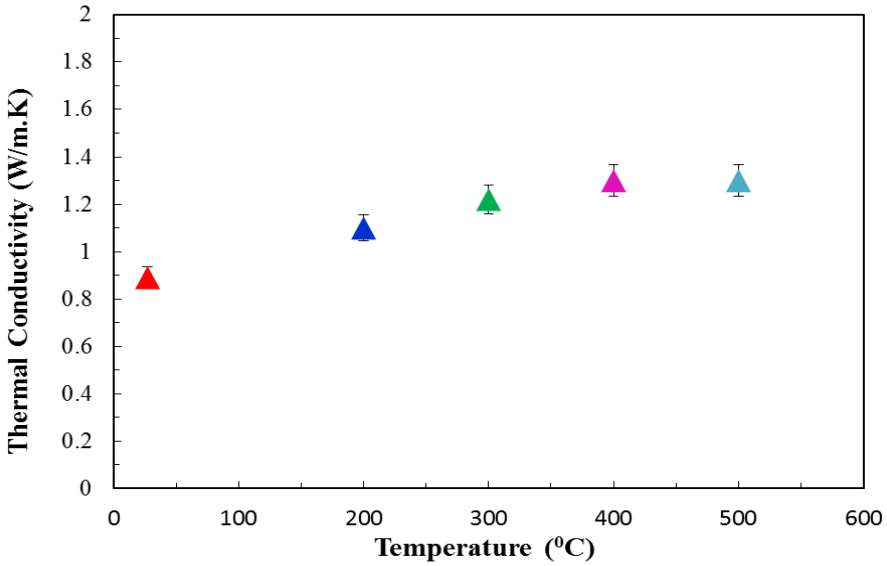

Figure 19: Variation of thermal conductivity of YSH coatings with temperature

Thermal conductivity of YSHZ coatings is plotted as a function of composition as shown in Figure 20. The compositional dependence of thermal conductivity is evident in the trend shown in Figure 9.27. While thermal conductivity of these YSHZ coatings in general, attains a lower value, the trend seen is an indicative of lower values towards 1:1 ratio of hafnia and zirconia in the coating. However, the thermal conductivity values slightly increases towards the end members where either hafnia or zirconia content is more than the other.

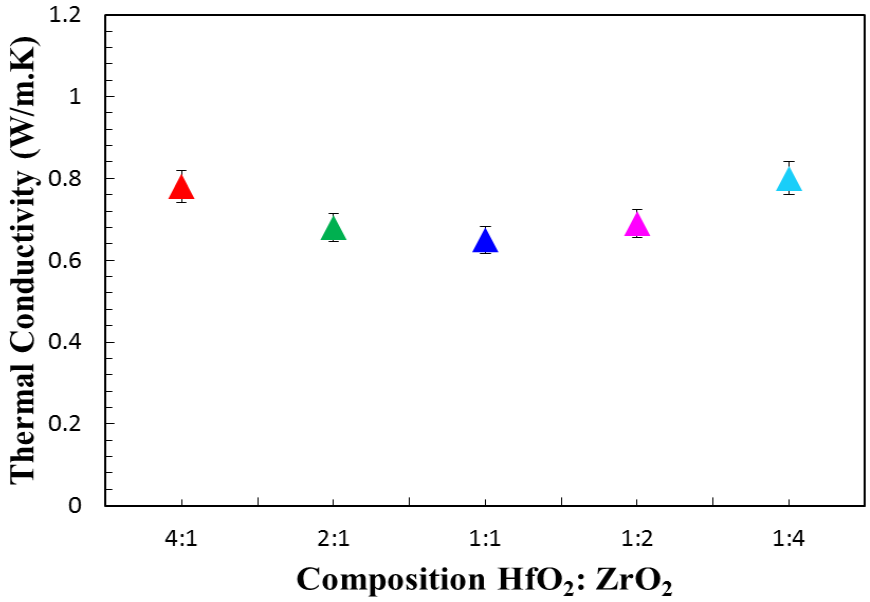

Figure 20: Thermal conductivity of YSHZ coatings as function of composition

Thermal conductivity analysis of the Gd_2O_3-HfO_2 coatings was also evaluated as a function of Gd_2O_3 content. Analysis of the data for extraction of thermal conductivities was accomplished with a frequency-domain model in which the ratio of the in-phase and out-of-phase lock-in amplifier signals is calculated as a function of time:

$$-\frac{V_{in}}{V_{out}} = \frac{\sum_{-m}^{m}\left(\Delta T\left(m/\tau + f\right) + \Delta T\left(m/\tau - f\right)\right)\exp\left(i2\pi mt/\tau\right)}{i\sum_{-m}^{m}\left(\Delta T\left(m/\tau + f\right) - \Delta T\left(m/\tau - f\right)\right)\exp\left(i2\pi mt/\tau\right)} \qquad (5)$$

Here m is an integer denoting summation over pump pulses, τ the time between unmodulated laser pulses (12.5 ns), f the modulation frequency (9.8 MHz), and t the time delay between pump and probe pulses. The variation of the thickness of the sample layers was taken into account for TDTR modeling purposes. In modeling the data, the volumetric heat capacities used for the sample layers were weighted averages (based upon the mol% of Gd_2O_3) calculated from the known quantities of 2.73 J cm^{-3} K^{-1} for HfO^2 [29,30] and 2.14 J cm^{-3} K^{-1} for Gd_2O_3 [31]. The samples were assumed fully dense when considering heat capacity estimates as a function of Gd_2O_3 concentration. For the samples studied, TDTR data were acquired from five locations on each sample surface. The scans were individually modeled, and an average thermal conductivity ± standard deviation value was calculated for each sample.

The results of the thermal conductivity measurements are shown in Figure 21, while examples of individual TDTR scans and data models are shown in the inset. The error bars from Figure 6 represent no more than 6 % uncertainty. A TDTR calibration sample (amorphous silicon dioxide at 1.3 W m^{-1} K^{-1}) yielded approximately 95 % accuracy. The value for pure HfO_2 (0 mol% Gd_2O_3) is plotted in Figure 21 for comparison, illustrating that the most striking feature is a significant drop in thermal conductivity with addition of Gd_2O_3. The measured value at room temperature for the 4 mol % Gd_2O_3 sample (1.7 ± 0.1 W m^{-1} K^{-1}) is lower than ZrO_2 samples doped with 4 mol % of either Y_2O_3 (~2.5 W m^{-1} K^{-1}) or Gd_2O_3 (~2.3 W m^{-1} K^{-1}) [32]. Hence, the Gd_2O_3-HfO_2 materials are better suited as thermal barrier coatings. Figure 21 also illustrates a trend of decreasing thermal conductivity with increasing Gd_2O_3 mol % (up to 12 mol %). Such an inverse trend of thermal conductivity with doping levels has previously been observed in Y_2O_3-ZrO_2 systems [21]. For the Gd_2O_3-HfO_2 materials studied here, the decrease in thermal conductivity with larger doping contents is consistent with oxygen vacancies playing the dominant role in phonon scattering [21]. These are structural vacancies in the hafnia due to charge compensation of Gd^{+3} ions substituting for Hf^{+4} ions. Another factor known to

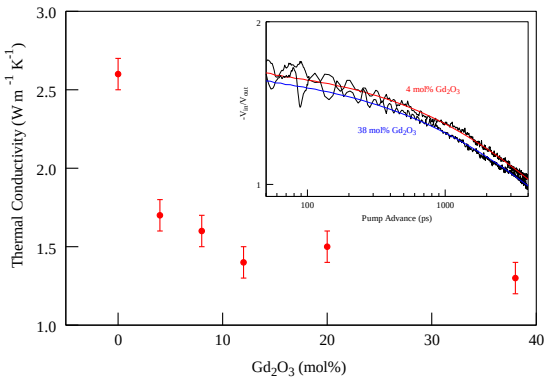

Figure 21: Thermal conductivity of GSH coatings.

influence thermal conductivity is grain size [21]. The morphology analysis indicated that coalescence to form larger grains resulted as the mol % of Gd_2O_3 increased, which would increase the thermal conductivity. This is because larger grains result in fewer grain boundaries which can scatter phonons. However, this trend was not observed in our results, thus supporting our hypothesis that oxygen vacancy effects predominantly govern thermal transport. Figure 21 also reveals a discontinuity in the thermal conductivity trend for Gd_2O_3 content higher than 12 mol%, which is possibly due to substantial increase of Gd^{3+} concentration and oxygen vacancies formation.

Thermal and Chemical Stability

The enhanced thermal stability of the coatings was found in high temperature XRD measurements. No phase or compositional change was observed in the YSH and YSHZ coatings by exposing to a temperature of 1300 ^{o}C. The stable cubic structure was retained after exposure to 1300 ^{o}C (Figure 22). The thermal-induced changes in the chemical composition are probed using the EDS measurements before and after thermal stability experiments (Figures 23). EDS indicates that the composition of the coatings is the same before and after thermal stability experiments. Thermo-chemical analysis based on the EDS measurement indicates the coatings' chemical stability to higher temperatures (1300 ^{o}C).

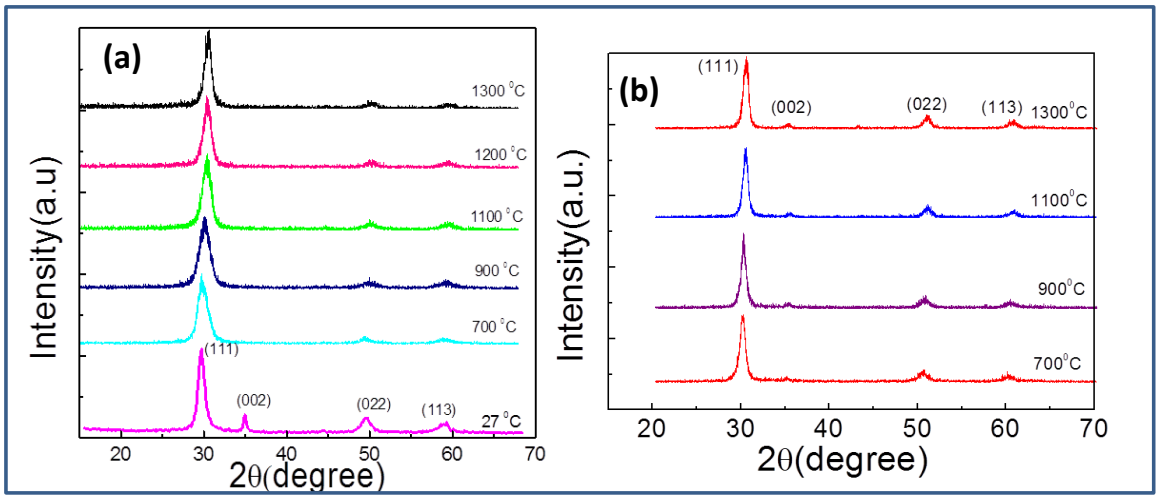

Figure 9.22: (a) High-temperature XRD curves of YSH coatings showing the phase-stability at 1300 ^{0}C; (b) High-temperature XRD patterns of representative YSHZ (HfO_2:ZrO_2 = 4:1) coatings showing the phase stability at 1300 ^{o}C

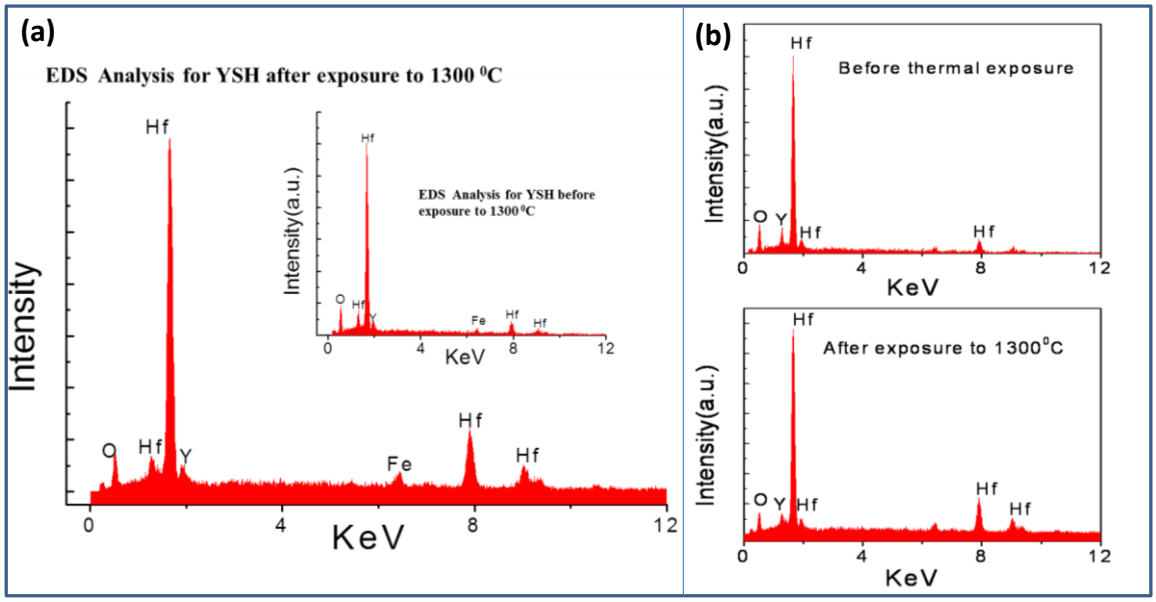

Figure 23: (a) EDS data of YSH coatings before and after thermal treatment at 1300 ^{o}C; (b) EDS data of YSHZ coatings before and after thermal treatment at 1300 ^{o}C.

Mechanical Properties

Hardness (H), modulus of elasticity (E_s), reduced modulus of elasticity (E_r) and stiffness (S) for YSH and various compositions of YSHZ coatings are shown in Figure 24. The stress versus displacement plot and optical images after nano-indentation were shown in Figure 25 for representative samples. It is evident (Fig. 24) that YSH presents the maximum value in all mechanical characteristics when compared to all other compositions. The optical images shown are representative of the indentations (Fig. 25).

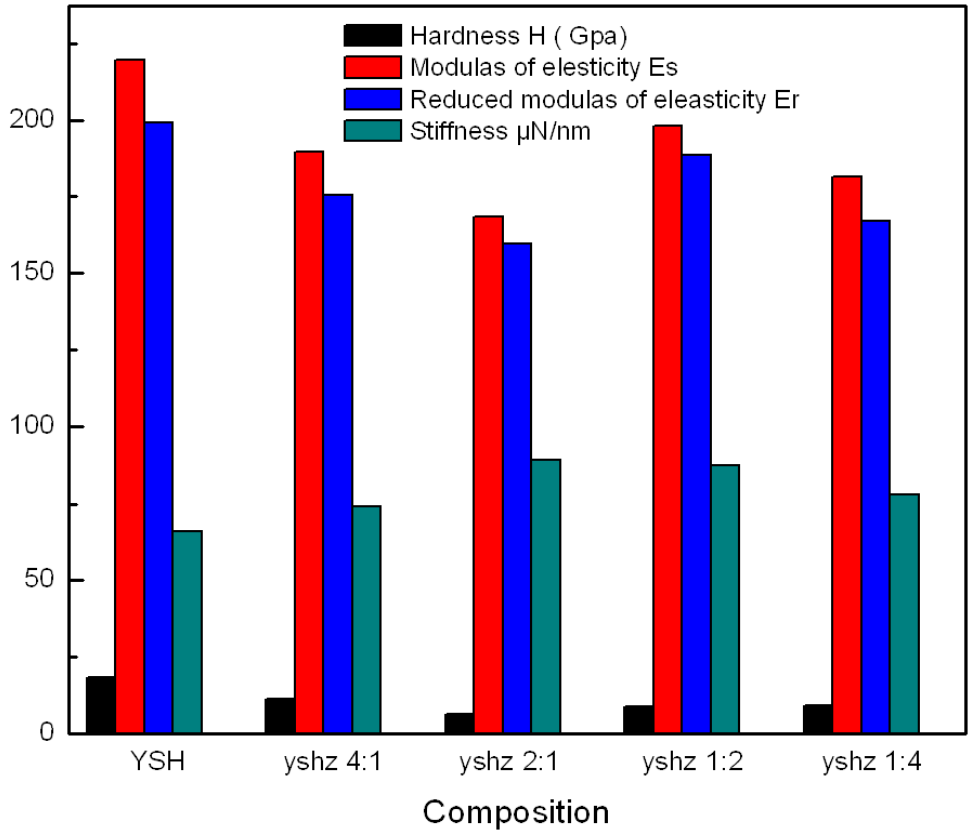

Figure 24: Mechanical properties of YSH and YSHZ coatings measured using nano-indentation

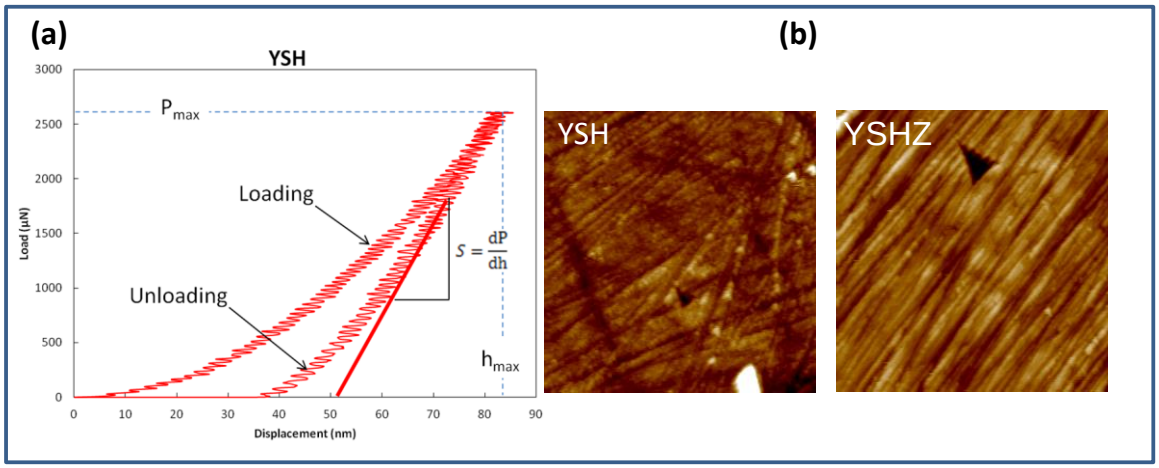

Figure 25: (a) Stress versus displacement plot for nano-indentation on YSH coating. (b) Optical images of YSH and YSHZ coatings after nano-indentation.

One of the most important microstructural parameters that influence the mechanical properties is grain size [24]. There is a critical grain size at which the mechanical properties e.g, Young modulus starts decreasing drastically [24]. This critical grain size

in pure Hafnia is ~2 µm. The focus in this work was towards nanostructured coatings. The grain size of YSH and YSHZ coatings employed for mechanical property evaluation are in the range of ~ 5-20 nm, which is quite low compared to the critical grain size where the mechanical properties degradation is noted in pure hafnia. No drastic change in mechanical properties with the variation of composition in YSHZ may actually be due to the fact the grain size extremely low to induced changes in mechanical characteristics. The interpretation of the mechanical properties could be based on the residual strain energy stemmed from the anisotropy of thermal expansion. If the grains are big enough, micro-cracks are initiated which is responsible for the reduction in mechanical strength. This is not the case in this work as no phase change apart from cubic structure was evident in the operating range of temperature (up to 1300 ^{o}C) which could the origin of significant thermal expansion anisotropy. Since there is no transformation toughening in either YSH or YSHZ coatings, the hardness, Young's modulus and stiffness values are the reflection of the combination of individual material properties of hania, zirconia and yttria. These properties in fully or partially stabilized hafnia or hafnia-zirconia mixed compositions are strongly influenced by the microstructure such as porosity and grain size. As the porosity was not investigated in this work, the quantitative influence of porosity on mechanical properties of YSH and YSHZ is not a matter of discussion here. The high value of hardness and Young's modulus is, perhaps, due to the dense columnar structure which is clearly seen in both YSH and YSHZ. As was reported, the hardness value of fully stabilized hafnia decreases with the content of alloying oxides. This observation is also visible here when zirconia is incorporated in YSH structure; YSHZ exhibits lower hardness values than YSH. Although the hardness and Young's modulus are very high and close to YSH, there is slight randomness among all the compositions of YSHZ. The randomness is due to the experimental uncertainty resulted due to the columnar structure of both YSH and YSHZ. The mechanical properties were measured using the nano-indentation on the surface of the samples. It is really hard to identify from the top of the surface exactly where the columns are located. If the nano-indenter is placed on the column it will show higher hardness value compared to that obtained if the indenter is placed in between the columns. Figure 26 presents the mechanical properties before and after exposure to 1300 ^{o}C used for high temperature XRD. YSH coatings show the similar mechanical properties before after exposure to 1300 ^{o}C indicating the high mechanical stability.

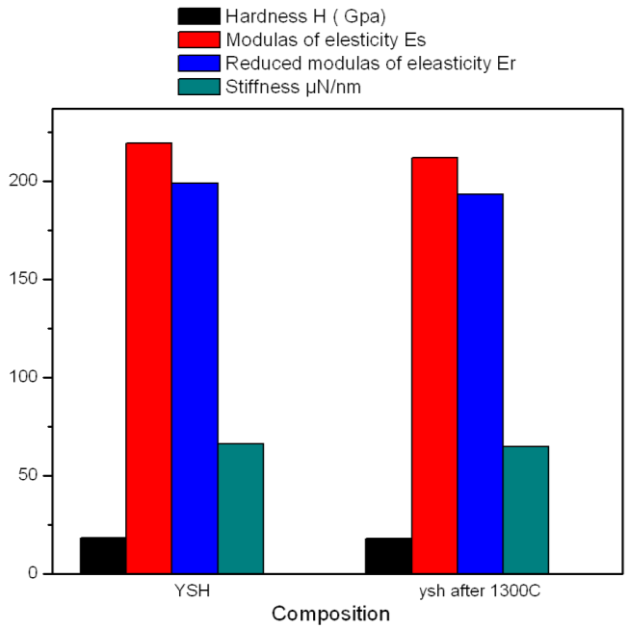

Figure 26: Mechanical properties of YSH coatings before and after exposure to 1300 ^{o}C

Residual Stress

Residual stress analysis was performed using the X-ray diffraction pattern analysis of the coatings as a function tilt angle (ψ). The well-known $\sin^2\psi$ method was adopted to calculate the residual stress [33,34]. The variation of d-spacing was measured using the diffraction of Cu-K_α radiation by higher angle planes. X-ray diffraction was carried out at various tilting angles. A linear relation is obtained between the inter-planner spacing and $\sin^2\psi$ values. A plot for YSH grown on Inconel-738 is shown in Figure 27. The data presented (Figure 27) shows the d-spacing as function of $\sin^2\psi$. Then the residual stress has been calculated using the well-known expression shown in eqn. 5. (20)

$$\frac{d_{\Phi\Psi} - d_0}{d_0} = \frac{1+\nu}{E}\sigma_\Phi \sin^2\Psi - \frac{\nu}{E}\sigma_{11} + \sigma_{22} \qquad (6)$$

The residual stresses calculated for YSH and YSHZ coatings are shown and compared in Figure 28. The effect of substrate materials on the residual stress of YSH coatings is also evaluated and presented in Figure 28. YSH shows the similar residual stress on both the SS-403 and inconel-738 substrates. The as grown YSH coating shows a compressive residual stress of ~ 2GPa on both the SS-403 and inconel-738 substrates. However, YSHZ shows lower residual stress compared to YSH which is less than 1 GPa. The existing reports as documented in the literature indicates that the residual stress of YSZ coatings ranges from few MPa to close to GPa depending on either processing conditions and coatings' microstructure [35,36]. While residual stress in YSH and YSHZ coatings in the present work is higher compared to traditional YSZ coatings, the behavior may not yield an idealistic behavior or unified model to account for the differences. The obvious reason is that the current set of experiments is designated to understand the stress evolution and behavior at the early stages of growth at the nano-to-submicron-to-micron level or at the interfaces. At such early stages, especially during the first few layers growth of the initial coating, a high level of residual stress state is expected than normal. Such a behavior is very common in all types PVD growth of coatings. Therefore, in the present case, since the thickness of the coating is not enough to overcome the substrate effect, a higher level of compressive stress is developed during the deposition of the coatings.

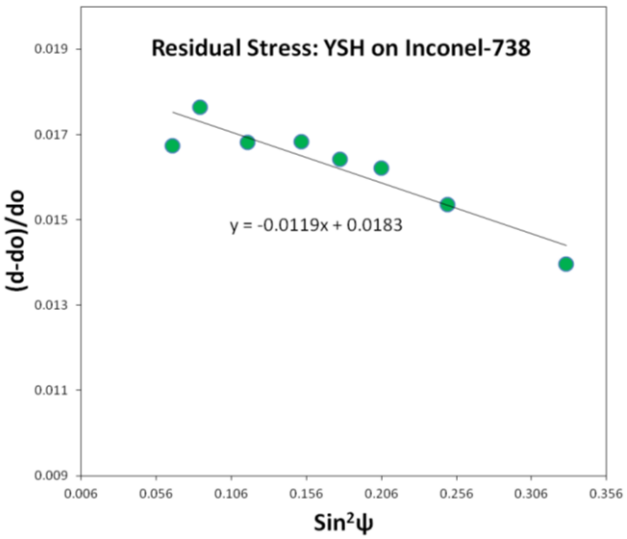

Figure 27: d-spacing as a function of $\sin^2\psi$ for YSH sample grown on Inconel-738

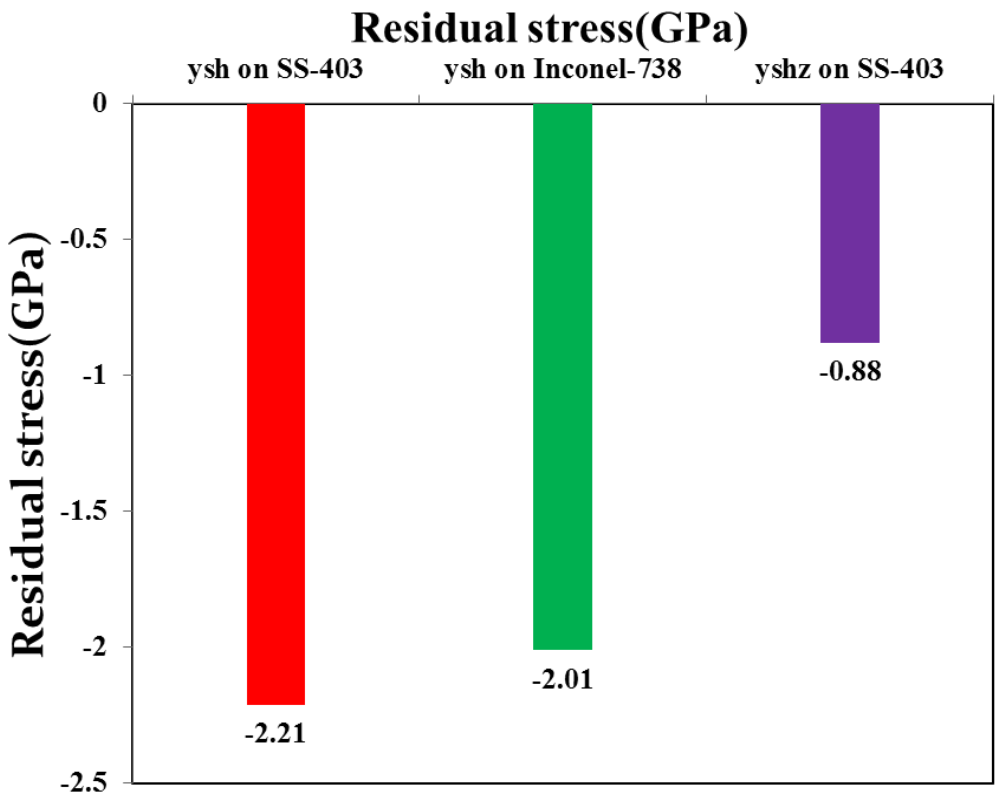

Figure 28: Residual stresses calculated for YSH and YSHZ coatings

Hot Gas Exposure

The hot gas exposure experiments were performed for extended duration (under variable time) at 1100 ^{o}C (the best available temperature without having the coating too close to the flame in the current design) for YSH coatings. After every span of hot gas exposure, microstructure and morphology were investigated. The details of the operating conditions are as indicated below in Table 3. The durability of the YSH, GSH and YSZH coatings was investigated by exposing the samples to hot gases produced by the combustion of CH_4 and Air. A swirl stabilized syngas combustor (Figure 29) was used for this purpose. The sample holder was designed in such a way that the impingement angle can be changed. Samples of different sizes can be accommodated by adjusting the threaded rod coupler. K-type thermocouple was used to measure the temperature near samples inside the combustion chamber.

Table 3: Details of hot gas exposure experiments

Conditions	**Composition of the coatings**	
	YSHZ	YSH
Used gases for combustion	CH_4 and air	CH_4 and air
Flow rate of CH_4	19.8 L/min	19.8 L/min
Flow rate of Air	198 L/min	198 L/min
Anticipated composition of the hot gases	CO, CO_2, N_2, O_2 and unburned hydrocarbons	CO, CO_2, N_2, O_2 and unburned hydrocarbons
Temperature of the hot gas	1000 ^{0}C	1000 ^{o}C
Exposure time	1-2 hr	1-2 hr
Angle of impingement	90^o	90^o

Figure 29: Combustor set-up employed to evaluate the coatings

XRD patterns of YSH coatings before and after exposure to hot gases are shown in Figure 30. No significant change in microstructure is noted. However, the strongest peaks show slight shift in the peak position towards the higher 2θ values with the increase of hot gas exposure time. The peak shift is indicated by drawing a line through the (111) peaks (Figure 30). This peak shift indicates the decrease in interplanar spacing with the increase of exposure time. Little change in orientation is evident after 9 hrs exposure to 1100 ^{o}C. The coatings show stronger orientation toward (002) direction rather than (111) direction. However, the coating material does not show any change from the cubic crystal structure.

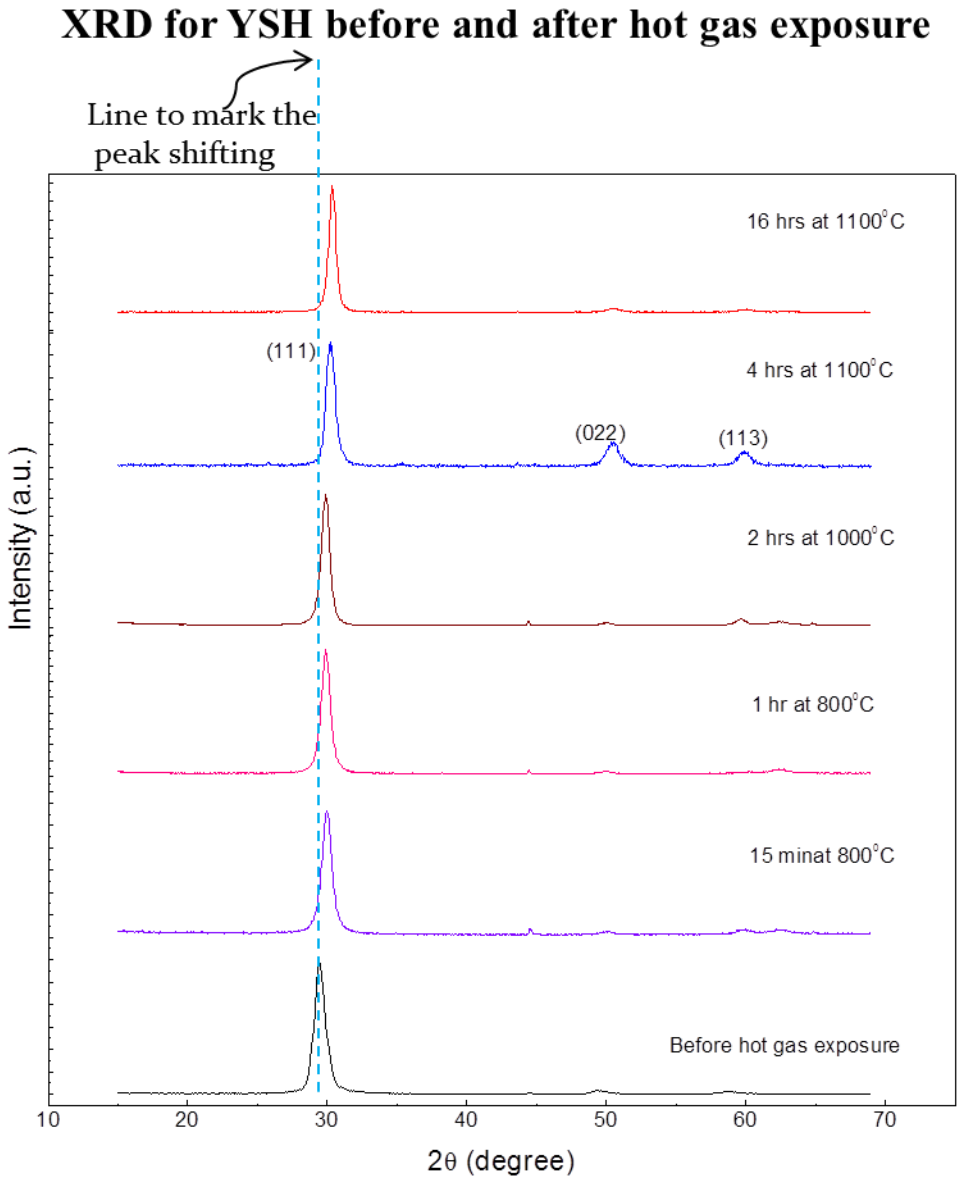

Figure 30: XRD patterns of YSH coating before and after exposure to hot gases.

The surface morphology of YSH coatings after exposure to hot gas is shown in Figure 31. No significant change other than slightly more compactness of the grains is visible from SEM images when the samples are subjected to hot gases for 9 hrs at 1100 ^{o}C. The

morphology after exposure for duration of 16 hrs at 1100 ^{o}C shows slightly different view. It is evident from Figure 31 that grains are more defined and packed dense.

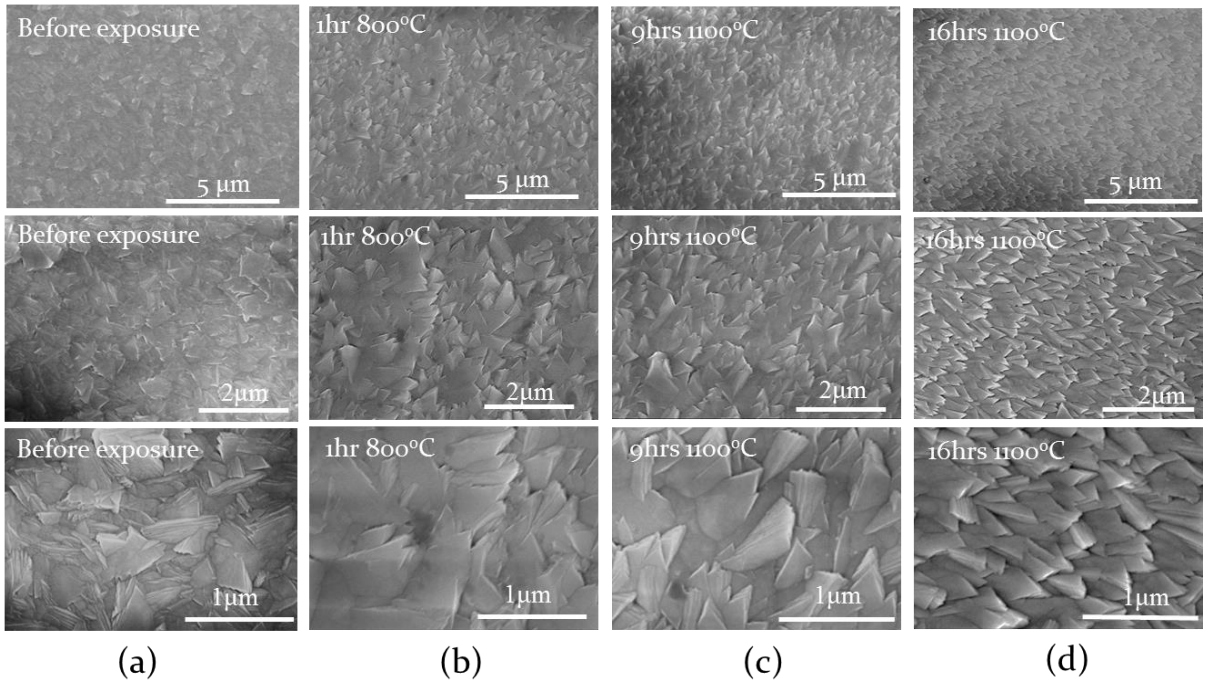

Figure 31: SEM images of YSH sample after exposure to hot gases

Residual stress after hot gas exposure:

Analysis of residual stress in the coatings was performed after performing the hot gas exposure experiment for a specific duration of time. Figure 32 shows the residual stress for YSH samples before and after exposure to hot gas. It is evident (Figure 32) that as grown YSH coating holds high residual stress within the coating. It is interesting to note that the coating shows a significant relaxation of residual stress through the exposure to hot gas within the short period of time, like 2 hours. However, the coating gains the stress back after exposure to hot gas at higher temperature for longer duration of time. Comparing the residual stress developed in the as grown coating, coating under hot gas for 9 hrs and the coatings under hot gas for 16 hrs exhibit more or less similar compressive stress, which is as high as around 2 GPa.

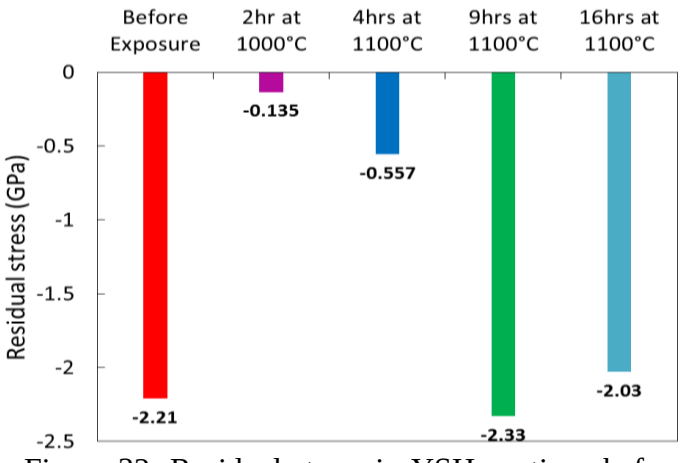

Figure 32: Residual stress in YSH coatings before and after exposure to hot gases

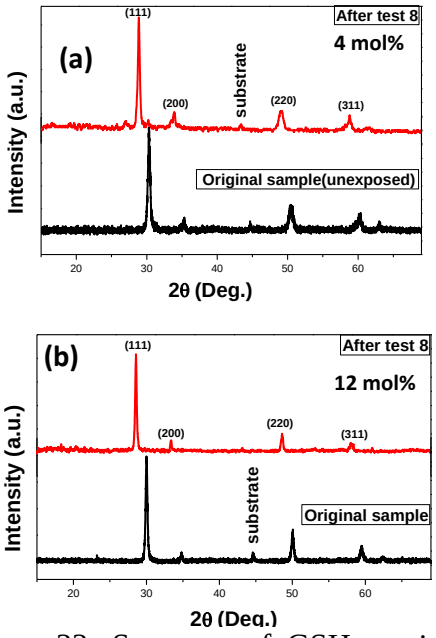

Figure 33: Structure of GSH coatings under hot gas exposure

The durability of the GSH coatings was also tested by exposing them to the hot gases. The XRD data of the representative GSH coatings after various tests are shown in Figure 33. Data shown are for 4 mol% and 12 mol% Gd_2O_3 content in the GSH coatings. The surface morphology of the coating remains unchanged. However, XRD analysis shows that the (111) peak shifts 1.45° left (Figure 33) compared to the original unexposed sample. The shifting of (111) peak was calculated after fitting the peak with a Gaussian function. The shifting of peak is due to the strain within the coating, which was developed upon thermal effects under hot gas exposure. The accumulation of the carbon particles on the surface from the product of combustion was detected from EDS analyses.

Thermal Oxidation

The results of thermal oxidation measurements indicate that the material exhibits a good resistance against oxidation at higher temperatures. The weight of the samples increases with the increase of exposure time but the extent of increment is low which is ~0.002 gm/cm^2 after 5 hours and ~0.025 gm/cm^2 after 160 hrs for the YSH samples grown by either sputtering or EBPVD deposition. The samples grown on alumina do not show any further oxidation after getting the weight increase of 0.009 gm/cm^2. The samples grown on SS-403 without bond coat indicate the highest amount of weight increase which is due to the oxidation of substrate material. The weight increase against the exposure time is shown in Figure 34, a) weight increase per unit area against exposure time and b) total weight increase against exposure time.

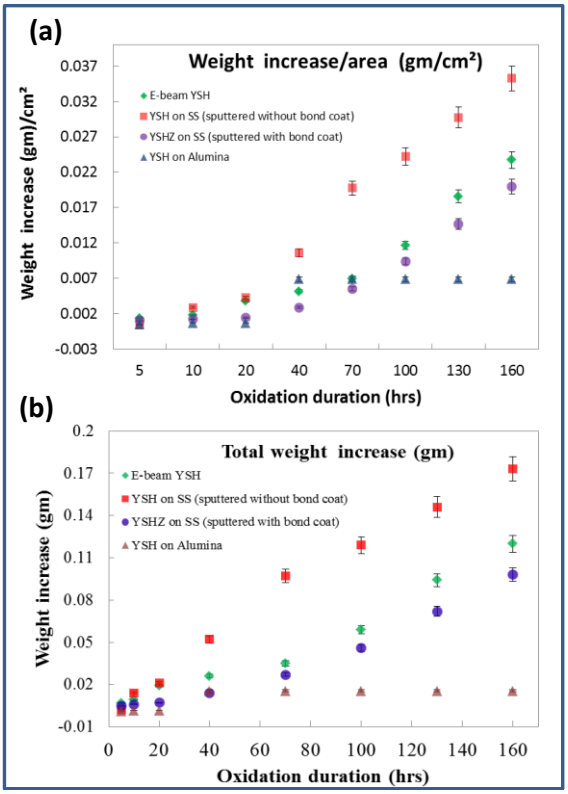

Figure 34: The weight increase against the exposure time. a) weight increase per unit area against exposure time and b) total weight increase against exposure time

The interface at the bond coat - top coat was investigated using crosssectional SEM and TEM imaging analysis. No interface between bond coat and topcoat was visible when YSH coating was grown on inconel-738. Figure 35 shows the crosssectional images of YSH coating on bond coat (NiCoCrAlY) examined by SEM. A careful examination of SEM images shown in Figure 35 indicates that the interface morphology in one image is different from another. This is because of the fact that the crosssectional sample was prepared after deposition of the top coat. After the deposition of YSH on Inconel-738, the sample was mounted vertically in the epoxy polymer. After mounting, the top surface was polished in order to get the smooth surface on one edge. The area where the top coat was polished perfectly looks like plane (top right picture) and the area where the polishing could not touch the topcoat or made little abrasion looks like the picture place in bottom right position of Figure 35. The top coat might be delaminated in some areas (eg, bottom left image) because of the uneven abrasion during the polishing. The images are presented for a comparison purpose. Figure 36 shows the cross-sectional images of YSH coating on alumina substrate obtained by TEM.

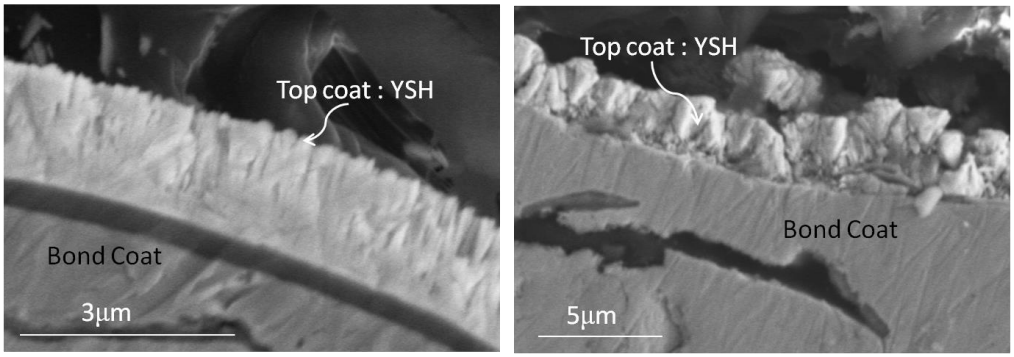

Figure 35: Crosssectional images of YSH coatings on bond coat (NiCoCrAlY) obtained by SEM.

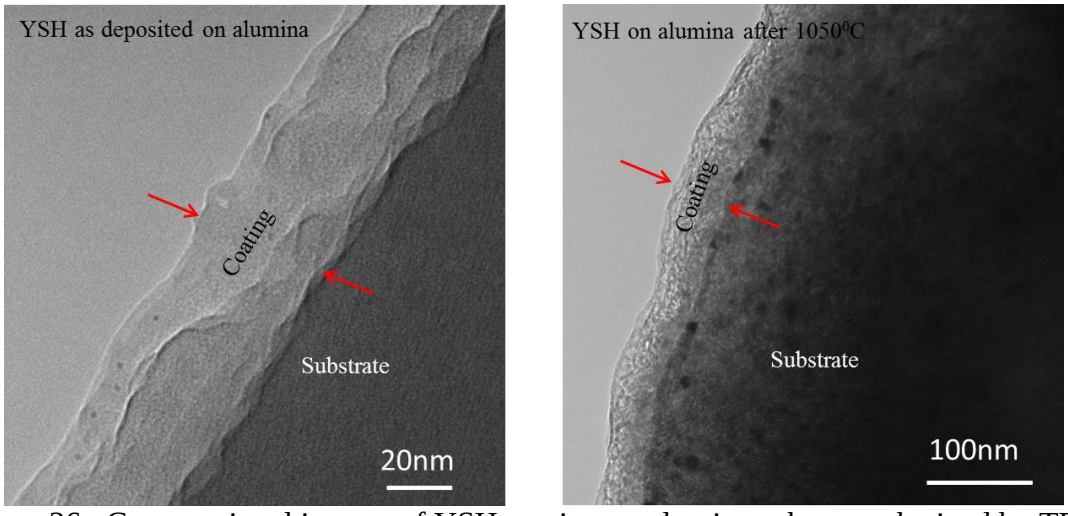

Figure 36: Crosssectional images of YSH coating on alumina substrate obtained by TEM

EBPVD Coatings

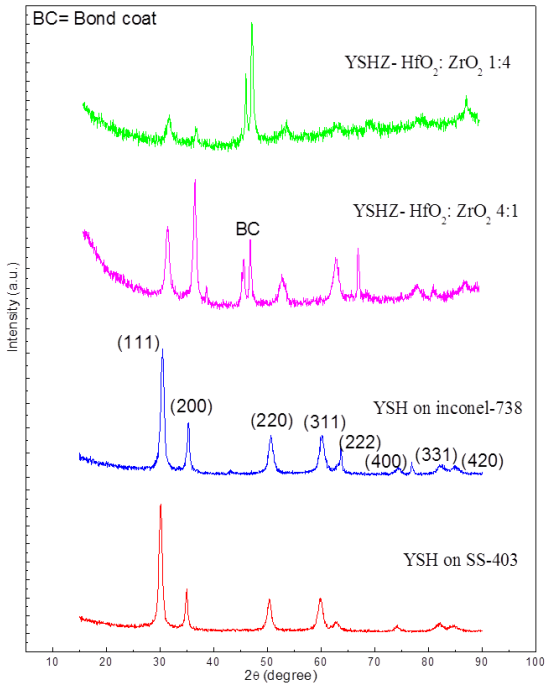

Figure 37: XRD patterns of EBPVD grown YSH and YSHZ coatings

YSH and YSHZ coatings were grown using EBPVD. The crystal structure and morphology of these coatings was investigated employing XRD and SEM analyses, respectively. The XRD patterns of YSH and YSHZ coatings grown by EBPVD are shown in Figure 37. The XRD data indicates that both the YSH and YSHZ coatings crystallize in cubic structure. YSH coatings grown on either SS-403 or Inconel-738 exhibit the preferred orientation along (111) direction of cubic hafnia. YSHZ coatings with the hafnia to zirconia ratio of 4:1 indicates a strong orientation towards (200) direction of cubic hafnia. On the other hand, when zirconia content is four times more than hafnia the peaks are less intense and the interaction from the bond coat is dominant. The bond coat peaks were labeled as BC.

The SEM data of EBPVD YSH coatings is shown in Figure 38. The images shown are for samples fabricated on SS-403 (upper panel) and Inconel-738 (lower panel). It is evident (Figure 38) that YSH grows vertically and agglomerates in big particles (left panel). Images were obtained at higher magnification to see the grain orientation.

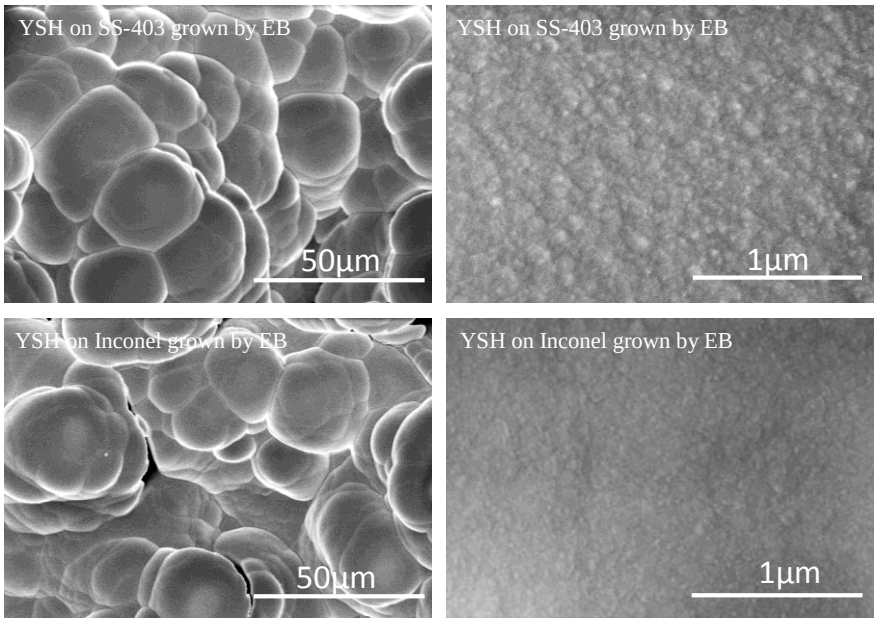

Figure 38: Surface morphology of YSH coatings grown by EBPVD

The SEM images of YSHZ-1 and YSHZ-4 coatings grown by EBPVD are shown in Figure 39. It is evident that both the YSHZ-1 and YSHZ-4 agglomerate in large particles, which are condensed in dense structure. The average particle size is slightly higher when hafnia is more than zirconia in the coating compared to that when hafnia is less than zirconia. It is also evident from the high magnification images (Figure 38; right panel) that the small grains are randomly distributed within the bigger particles. However, the grains are not clearly visible from theses SEM images.

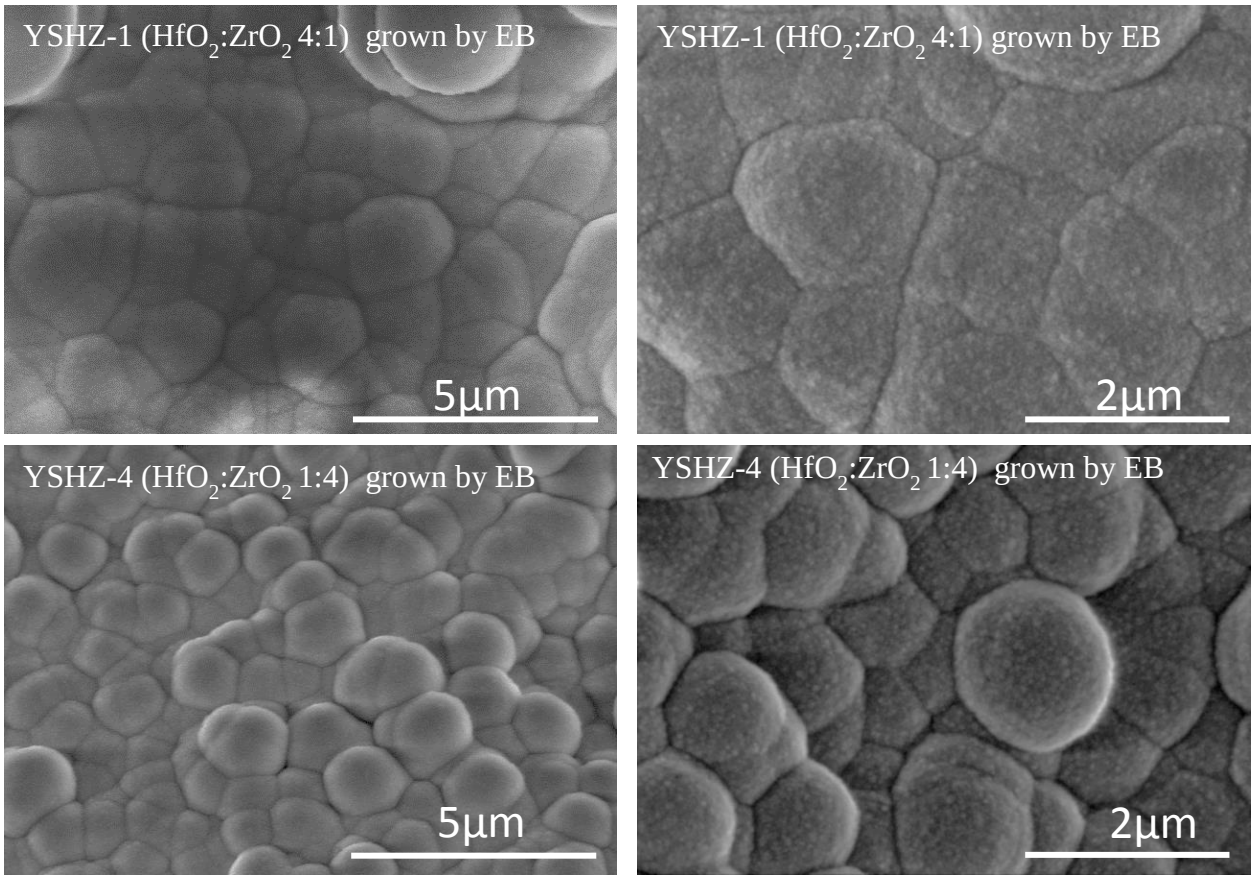

Figure 38: Surface morphology of YSHZ-1 and YSHZ-4 coatings grown by EBPVD

Very clear and well developed grains were visible when the samples were annealed at 900 ^{o}C for 15 hrs as shown in Figure 39. Because of the high temperature, the grains are looked to be attached to each other.

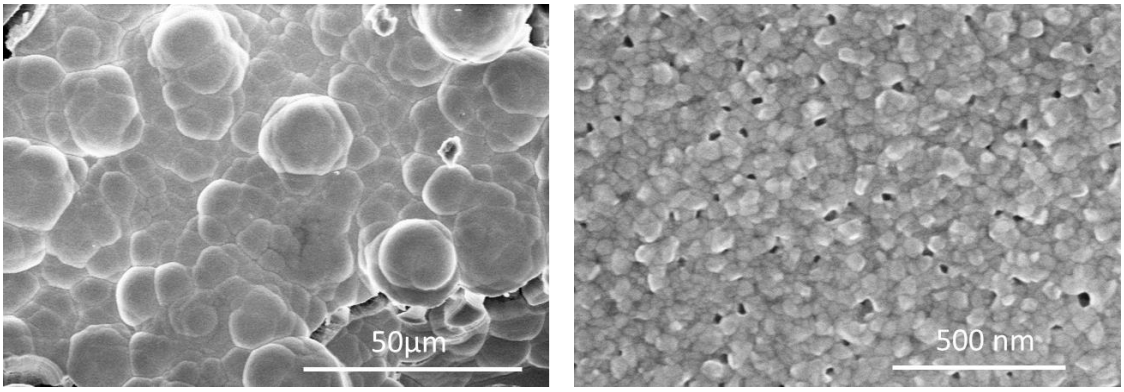

Figure 39: Surface morphology of YSH coatings grown by EBPVD after annealing at 900 ^{o}C for 15 hrs

Figure 40 shows the cross-sectional SEM images of YSHZ samples grown by EBPVD as a representative sample. The crosssectional image shows the columnar growth of the YSHZ coatings when grown by EBPVD technique. The upper portion of the columns looks wide and stressed compared to the bottom part. Coatings were grown on Si without bond coat in order to get the cross-sectional images. It was evident from the sample surface that the coating was partially delaminated from the substrate was bent upward. That's why the upper portion of the coating looks like stressed.

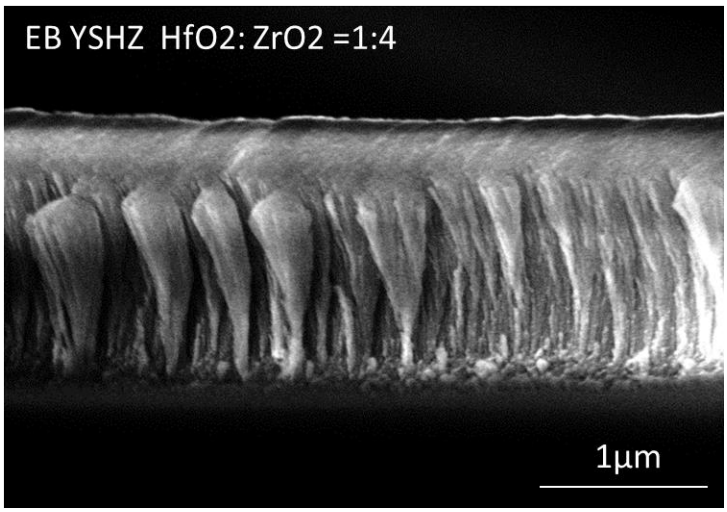

Figure 40: The crosssectional SEM images of YSHZ samples

Thermal Cycling

The thermal cycling experiments were performed on the pellets prepared using various compositions of hafnia and zirconia keeping the yttria content constant at 7.5%. Five different compositions of hafnia and zirconia ranging 4:1, 2:1, 1:1, 1:2 and 1:4 were used for the thermal cycling experiment. 1hr cycle was used taking 10 minutes for ramping the temperature to 1300 ^{o}C, keeping 40 minutes at that temperature and 10minutes for cooling to the room temperature. Total 100 cycles were used for the experiment.

Microstructure has been investigated after the thermal cycling experiment. The XRD pattern indicates mixed phases of cubic and monoclinic structure as shown in Figure 9.49. All the compositions show similar structure, however the orientation looks little different when one composition is compared to other. The XRD pattern is more or less similar to that of the YSH coating exposed to high temperature (1100 ^{o}C -1500 ^{o}C).

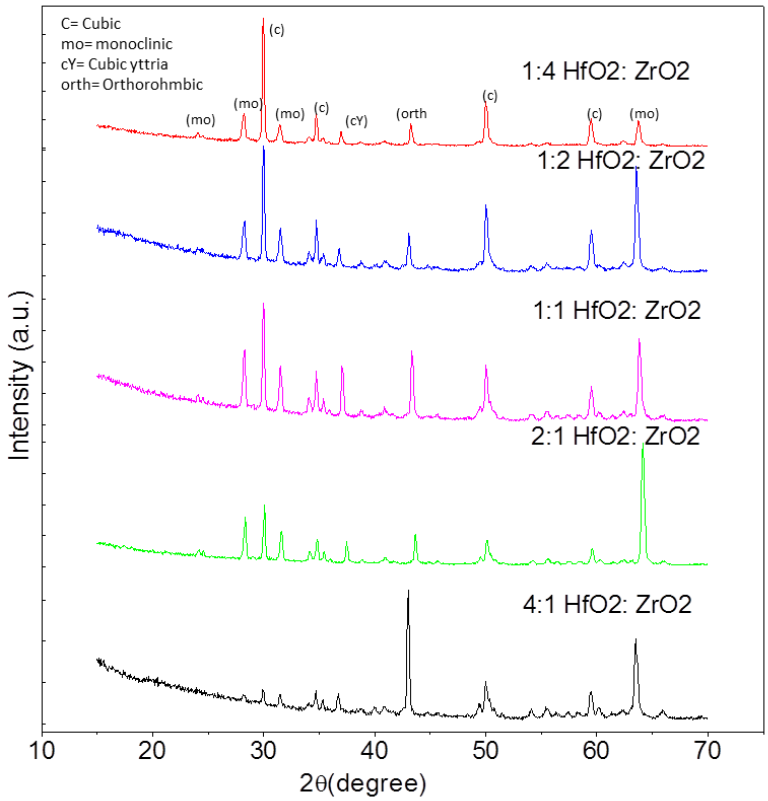

Figure 41: XRD pattern of the yshz pellets after 100 cycles of thermal cycling at 1300^{0}C

High Temperature Furnace Heating of YSH and YSHZ Coatings

The XRD patterns of YSZH subjected to isothermal oxidation for 24 hours at 1100 ^{o}C are shown in Figure 42. The structural stability of the YSZH is evident from the data set (Figure 42). The XRD patterns of YSH coatings after exposure to high temperature are shown in Figure 43 and 44. YSH and various compositions of YSHZ coatings were grown on alumina substrates in order to perform the high temperature furnace heating experiments. The YSH coatings were exposed to 1300^{0}C - 1500^{0}C for 12 hrs in an atmospheric furnace. YSHZ coatings of all five compositions grown on alumina were

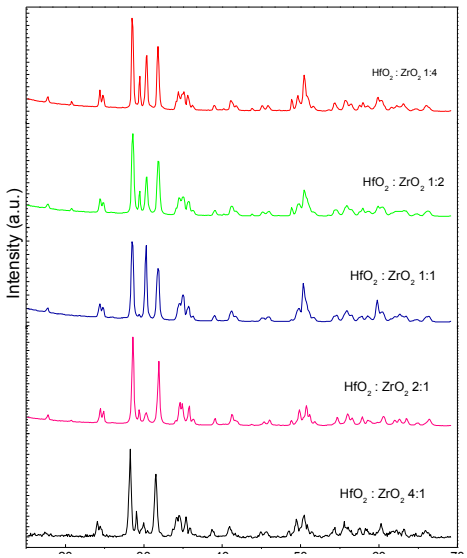

Figure 42: XRD patterns of YSHZ

exposed to 1300 ^{o}C for 12 hrs. The blank alumina substrate without any coating was also exposed to 1300 ^{o}C to investigate if any oxide is formed by the high temperature oxidation. The XRD pattern clearly shows that there exists a phase which is not form the coatings as the same peak appears at a 2theta value of about 42 degree. This was also confirmed by the grazing incidence XRD. When XRD was performed on the samples no appearance of this extra peak was visible. Excluding this extra peak the coatings show prominent cubic crystal structure of hafnia, however, some of the compositions show very mild appearance of monoclinic structure after exposure to 1300 ^{o}C for 12 hrs.

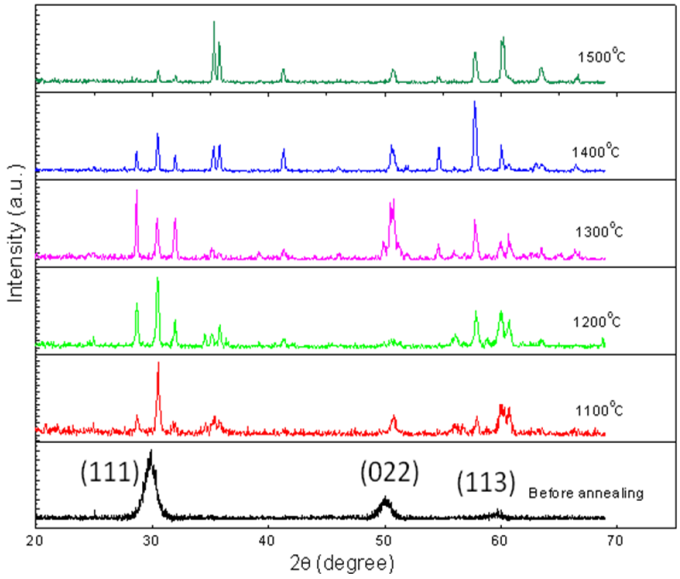

Figure 43: XRD pattern of YSH coatings after anealinng up to 1500 ^{0}C

Investigation of Gd_2O_3-HfO_2 Pellets:

The crystal structure of the Gd_2O_3-HfO_2 ceramics showed interesting structural evolution as a function of Gd_2O_3 content. XRD patterns of the Gd_2O_3-HfO_2 ceramics are shown in Figure 9.52 and 9.53. The formation of both monoclinic and fluorite phases is evident from the XRD curves (Figure 9.52 and 9.53) for Gd_2O_3 concentration increasing from 4 to 20 mol%, at which point there is no evidence of monoclinic phase. Gd_2O_3-HfO_2 ceramics with 20 mol% Gd_2O_3 exhibit only the fluorite phase. At 38 mol%, face centered cubic (fcc) pyrochlore $Gd_2Hf_2O_7$ (a =5.258 Å, JCPDS No. 24-0425) formation occurs.

With the increase of Gd_2O_3 concentration from 4 to 38 mol%, the structure is changing from both monoclinic and fluorite to single fluorite and finally to fcc pyrochlore. When the Gd_2O_3 concentration is 100 mol% (pure Gd_2O_3), the crystal structure was base-centered monoclinic (a=14.061 Å, b=3.566 Å and c=8.76 Å, JCPDS No. 43-1015) which is different from Gd_2O_3 powder pattern obtained at RT. The two phases (monoclinic + fluorite) region from 4-12 mol% Gd_2O_3 can be viewed as partially stabilized HfO_2 because there is not enough Gd^{3+} ions to fully stabilize the HfO_2. At 20 mol% Gd_2O_3, there are enough Gd^{3+} ions to stabilize the HfO_2 fully and thus a single fluorite structure is formed. At 38 mol%, there are more Gd^{3+} ions to form the pyrochlore composition and thereby forming fcc pyrochlore structure.

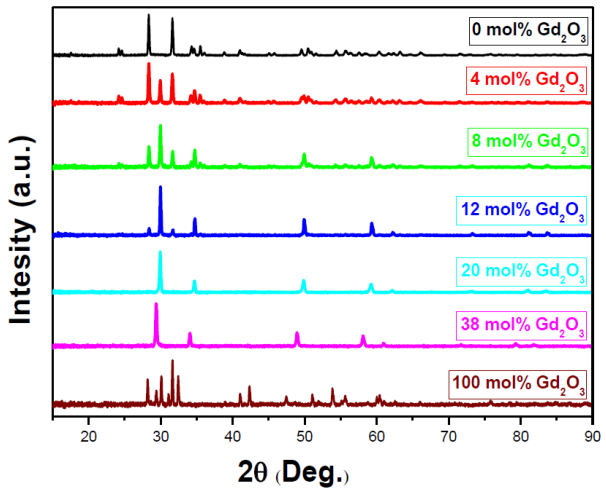

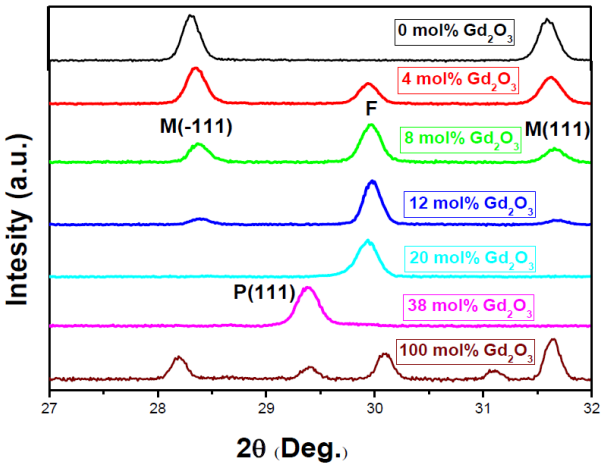

Figure 44 (top panel): XRD patterns of GSH pellets sintered at 1400 ^{0}C for 24 hours.
Figure 45 (lower panel): XRD patterns of GSH pellets sintered at 1400 ^{0}C for 24 hours.

Impact

Technical

A. Presentations

The following technical papers were presented at various meetings in addition to the annual UTSR workshops.

	Title	Author	Conference	Status
1.	Growth and Microstructure Analysis of Hafnia-Based Nanostructured Coatings	M. Noor-A-Alam Chandan K. Roy Christopher M. Bradely A.R. Choudhuri C.V. Ramana	AVS International Meeting, Albuquerque, NM Oct. 17-21, 2010	Presented
2.	Development of Hafnia Based Thermal Barrier Coating and its Microstructural Analysis	M. Noor-A-Alam Chandan K. Roy C. M. Bradley A. R Choudhuri C. V. Ramana	TMS Annual Meeting, San Diego, CA Feb. 27-March 3, 2010	Presented
3	Effect of Composition on the Growth and Microstructure of Hafnia-Zirconia Based Thermal Barrier Coatings	M. Noor-A-Alam A. R Choudhuri C. V. Ramana	ICMCTF, San Diego, CA May 2-6, 2011	Presented
4.	Microstructure and thermal stability of hafnia-zirconia based thermal barrier coatings	M. Noor-A-Alam A. R Choudhuri C. V. Ramana	IECEC July 31- Aug 3, 2011, San Diego, CA	Presented
5.	High-Temperature Tolerance and Chemical Stability of Yttria-Stabilized Hafnia,	M. Noor-A-Alam A. R Choudhuri C. V. Ramana	Southwest Energy Science and Engineering Symposium, April 16, 2011 El Paso, Texas	Presented
6.	Investigation Of Thermal Conductivity And Mechanical Properties Of Hafnia-Zirconia Based Thermal Barrier Coatings	M. Noor-A-Alam A. R Choudhuri C. V. Ramana	Southwest Energy Science and Engineering Symposium, March 24th, 2012, El Paso, Texas	Presented

B. Publications

The following papers were published in journals of science and engineering:

1. M. Noor-A-Alam, A.R. Choudhuri, C.V. Ramana; Effect of composition on the growth and microstructure of hafnia–zirconia based coatings; Surface & Coatings Technology, 206, 2011, 1628-1633

2. M. Noor-A-Alam, C.V. Ramana, Structure and thermal conductivity of yttria-stabilized hafnia ceramic coatings grown on nickel-based alloy; Ceramics International 38 (2012) 2957

3. C. V. Ramana, M. Noor-A-Alam, Jamie J. Gengler and John G. Jones; Growth, Structure, and Thermal Conductivity of Yttria-Stabilized Hafnia, ACS Applied Materials and Interfaces 4 (2012) 200−204

4. C. K. Roy, M. Noor-A-Alam, A.R. Choudhuri, C.V. Ramana; Synthesis and microstructure of Gd_2O_3-doped HfO_2 ceramics, Ceramics International 38 (2012) 1801–1806

5. Crystal Structure, Phase Analysis, and Thermal Conductivity of Nanocrystalline Gd_2O_3–HfO_2 Coatings, C. V. Ramana, Jamie J. Gengler, and John G. Jones, J. Phys. Chem. C 116 (2012) 25178–25183.

6. M. Noor-A-Alam, C.V. Ramana, Thermal conductivity of yttria-stabilized hafnia thermal barrier coatings grown on stainless steel alloy SS-403, Journal of Nanotechnology in Engineering and Medicine (in press)

7. E.J. Rubio, M. Noor-A-Alam, C.V. Ramana, Microstructure and thermal oxidation behavior of yttria-stabilized hafnia coatings grown on alumina, Surface and Coatings Technology (2013) revised version submitted to journal.

IV. CONCLUSIONS

YSH, YSZH and GSH coatings were fabricated with variable composition. Characterization of the materials was performed by microstructural analysis, evaluation of thermal conductivity and investigation of physico-chemical and thermo-mechanical properties. Durability tests were also performed in the laboratory combustor rig. Yttria stabilized hafnia (YSH) and yttria stabilized hafnia-zirconia (YSHZ) coatings crystallizes in cubic structure when grown by PVD methods. The crystal structrue and interface columanr structure of the coatings, which was evident from XRD and SEM analyses, was stable under thermal treatment of the coatings to a temperature of 1300 ^{o}C. Chemical composition and morphology also were maintained well in the coatings after exposure to 1300 ^{o}C. YSH coatings exhibit lower thermal conductivity compared to YSZ and HfO_2. Thermal conductivity of YSH coatings slightly increases with temperature while the coatings exhibit stability under hot gas exposure. Yttria-stabilization of hafnia in cubic phase significantly lowers the effective thermal conductivity compared to pure monoclinic hafnia. The thermal conductivity of nanocrystalline cubic YSH is 1.31 ± 0.03

$Wm^{-1}K^{-1}$. The effective reduction in thermal conductivity of YSH films is promising to utilize these materials in high temperature applications. The effect of Gd_2O_3 concentration on the crystal structure is remarkable. The Gd_2O_3 addition into HfO_2 matrix shows presence of fluorite phase and with the increase of Gd_2O_3 concentration. When Gd_2O_3 concentration is 20 mol%, single fluorite phase is formed and monoclinic phase is disappeared completely. XRD analysis of the GSH coatings indicates that the Gd_2O_3 addition stabilizes the cubic phase of HfO_2 and with the increase of Gd_2O_3 concentration the coating composition is changing to fcc pyrochlore. The grains are highly oriented along the (111) plane. For the Gd_2O_3-HfO_2 materials studied here, the decrease in thermal conductivity with larger doping contents is consistent with oxygen vacancies playing the dominant role in phonon scattering. These are structural vacancies in the hafnia due to charge compensation of Gd^{+3} ions substituting for Hf^{+4} ions. The morphology analysis indicated that coalescence to form larger grains resulted as the mol% of Gd_2O_3 increased, which would increase the thermal conductivity. This is because larger grains result in fewer grain boundaries which can scatter phonons. However, this trend was not observed in our results, thus supporting our hypothesis that oxygen vacancy effects predominantly govern thermal transport.

V. REFERENCES

1. D. Zhu, R.A. Miller, Int. J. Appl. Ceram. Technol. 1 (2004) 86-94.
2. S. Bose, J. DeMasi-Marcin, J. Therm. Spray. Techn. 6 (1) (1997) 99-104.
3. W.P. Parks, E.E. Hoffman, W.Y. Lee, I. G. Wright, J. Therm. Spray. Techn. 6 (2) (1997) 187-192.
4. W.P. Danesi, M. Semchyshen, in: C.T. Sims, W.C. Hagel (eds), The superalloys, John Wiley & Sons, New York, 1972, pp. 565-574.
5. N.P. Padture, M. Gell and E.H. Jordan, Science. 296 (2002) 280-284.
6. K. Matsumoto, Y. Itoh, T. Kameda, Sci. Technol. Adv. Mat. 4 (2003)153-158.
7. A.H. Heuer, L.W. Hobbs, in: Advances in Ceramics, Vol. 3, American Ceramic Society, Ohio, 1981, 241-251.
8. W. Ma, D. Mack, J. Malzbender, R. Vaben, D. Stover, J. Eur. Ceram. Soc. 28 (2008) 3071–3081.
9. R.S. Lima, B.R. Marple, Mater. Sci. Eng. A. 485(1–2) (2008), 182-193
10. L.L. Shaw, D. Goberman, R. Ren, M. Gell, S. Jiang, Y. Wang, T.D. Xiao, P.R. Strutt, Surf. Coat. Tech. 130 (1) (2000) 1–8.
11. M. Gell, E.H. Jordan, Y.H. Sohn, D. Goberman, L. Shaw, T.D. Xiao, Surf. Coat. Tech. 146-147 (2001) 48-54.
12. R. Soltani, H. Samadi, E. Garcia, T.W. Coyle, SAE Technical Paper. 2005-01-0650, 2005.
13. M. Gell, Nanostruct. Mater. 6 (1995) 997-1000.
14. M. Gell, Mater. Sci. Eng. A. 204 (1995) 246-251.
15. R.S. Lima, A. Kucuk, C.C. Berndt, Mater. Sci. Eng. A. 327 (2002) 224–232.
16. R.S. Lima, A. Kucuk, C.C. Berndt, Mater. Sci. Eng. A 313 (2001) 75–82.
17. Y. Zeng, S.W. Lee, L. Gao, C.X. Ding, J. Eur. Ceram. Soc. 22 (2002) 347-351.
18. H. Chen, C. X. Ding, Surf. Coat. Tech. 150 (2002) 31-36.
19. G. Soyez, J.A. Eastman, L.J. Thomson, G.R. Bai, P.M. Baldo, A.W. McCormick, R.J. DiMelfi, A.A. Elmustafa, M.F. Tambwe, D.S. Stone, Appl. Phys. Lett. 77 (2000), 1155-1157.
20. R.S. Lima, A. Kucuk, C.C. Berndt, Surf. Coat. Technol. 135 (2001) 166–172.
21. S. Raghavan, H. Wang, R.B. Dinwiddie, W.D. Porter, M.J. Mayo, Scripta. Mater. 39 (8) (1998) 1119–1125.
22. D. R. Clarke, S. R. Phillpot, Mater. Today. 8 (2005) 22-29.
23. C. K. Lee, E. Cho, H. S. Lee, C. S. Hwang, S. Han, Phys. Rev. B, 78 (2008) 12102 (1-4).
24. J. Wang, H. P. Li, R. Stevens, J. Mater. Sci. 27 (1992) 5397-5430.
25. D. W. Stacy, D. R. Wilder, J. Am. Ceram. Soc. 58 (1975) 285-288.
26. K.I. Portnoi, I.V. Romanovich, E. N. Timofeeva, Inorg. Mater. 7 (1971) 783.
27. R. Ruh, H. J. Garrett, R. F. Domagala, N. M. Tallen, J. Am. Ceram. Soc. 51 (1968) 23-28.
28. A. Rosencwaig and A. Gersho, J. Appl. Phys. 47 (1976) 64–69.
29. M. R. Winter, D. R. Clarke, Acta Mater. 54 (2006) 5051–5059.
30. C. Wang, M. Zinkevich, F. Aldinger, J. Am. Ceram. Soc. 89 (2006) 3751-3758.
31. R.J.M. Konigs, J.C. van Miltenburg, A.C.G. van Genderen, J. Chem. Thermodyn. 37 (2005) 1219-1225.

32. M.N. Rahaman, J.R. Gross, R.E. Dutton, H. Wang, Acta Mater. 54 (2006) 1615-1621.
33. V. Teixeiraa, M. Andritschky, W. Fischer, H. P. Buchkremer, D. StoÈver, J. Mater. Proc. Technol. 92-93 (1999) 209-216.
34. C. H. Ma, J. H. Huang, H. Chen, Thin Solid Films 418 (2002) 73–78.
35. D. J. Quinn, B. Wardle, S. M. Spearing, J. Mater. Res. 23 (2008) 609-618.
36. J. Matejicek, S. sampath, P. C. Brand, H. J. Prask, Acta Mater. 47 (1999) 607-617.